RESEARCH ARTICLE

Mapping human visual contrast sensitivity and vision loss across the visual field with model-based fMRI

Hugo T Chow-Wing-Bom[1,2]*, Matteo Lisi[3], Noah C Benson[4], Freya Lygo-Frett[5], Patrick Yu-Wai-Man[1,6,7,8], Frederic Dick[2,9], Roni O Maimon-Mor[1], Tessa M Dekker[1,2,9]

[1]Institute of Ophthalmology, University College London (UCL), London, United Kingdom; [2]Birkbeck/UCL Centre for NeuroImaging, London, United Kingdom; [3]Department of Psychology, Royal Holloway, University of London, London, United Kingdom; [4]eScience Institute, University of Washington, Seattle, United States; [5]Institute of Cognitive Neuroscience, UCL, London, United Kingdom; [6]John van Geest Centre for Brain Repair and MRC Mitochondrial Biology Unit, Department of Clinical Neurosciences, University of Cambridge, Cambridge, United Kingdom; [7]Cambridge Eye Unit, Addenbrooke's Hospital, Cambridge University Hospitals NHS Foundation Trust, Cambridge, United Kingdom; [8]Moorfields Eye Hospital NHS Foundation Trust, London, United Kingdom; [9]Department of Experimental Psychology, UCL, London, United Kingdom

***For correspondence:** hugo.chow-wing-bom.15@ucl.ac.uk

Competing interest: See page 22

Funding: See page 22

Preprint posted
17 December 2024
Sent for Review
06 February 2025
Reviewed preprint v1
31 March 2025
Reviewed preprint v2
03 June 2026
Version of Record
02 October 2026

Reviewing Editor: Xilin Zhang, Key Laboratory of Brain, Cognition and Education Sciences, Ministry of Education, South China Normal University, China

© Copyright Chow-Wing-Bom *et al*. This article is distributed under the terms of the Creative Commons Attribution License, which permits unrestricted use and redistribution provided that the original author and source are credited.

eLife Assessment

Using fMRI-based pRF mapping, this **important** study presents a novel method for estimating visual field (VF) loss and potential restoration by analyzing contrast-sensitivity patterns in early visual cortex. The evidence supporting the main claims is **convincing**. This work will be of broad interest to researchers in vision and clinical vision, neuroscience, and brain imaging.

Abstract Peripheral vision is crucial for daily activities and quality of life, yet traditional measures of visual function like visual acuity primarily assess central vision. Visual field tests can evaluate peripheral vision but require extended focus and precise fixation, often challenging for patients with severe sight loss. Functional MRI (fMRI) with population receptive field (pRF) mapping offers a non-invasive way to map scotomas but relies on single contrast levels and accurate fixation. We developed an fMRI-based approach to measure contrast sensitivity across the visual field without requiring precise fixation. Combining large-field stimulation with varying spatial frequencies and contrast levels, and either pRF mapping or a structure-based retinotopic atlas, we modeled contrast sensitivity in the primary visual cortex (V1) over a large (40 deg) expanse of the visual field. In seven normally sighted participants, we characterized differences in V1 sensitivity across eccentricities and visual quadrants, finding reliable and reproducible patterns at individual and session levels. To test robustness to fixation variability, we investigated how varying levels of eye movement affected V1 sensitivity patterns in two participants: cortical sensitivity patterns were largely preserved despite eye movements, particularly at low spatial frequencies. This suggests our approach can accommodate several degrees of fixation instability, making it suitable for populations with unstable or biased fixation for whom visual field maps are harder to acquire behaviorally (e.g., patients with dense central scotoma or strabismus). Additionally, our method effectively visualized simulated and disease-linked sensitivity loss at the cortical level. Crucially, these results could be largely recovered using the structure-based retinotopic atlas, eliminating the need for pRF mapping and precise

fixation, although with reduced sensitivity. This approach, integrating large-field stimulation with a retinotopic atlas, offers a promising tool for monitoring vision loss and recovery across a range of visual impairments, addressing a significant challenge in current clinical assessments.

Introduction

At least 2.2 billion people worldwide experience blinding eye diseases that emerge or progress across the lifespan, with 1.1 billion living with vision loss in 2020 (***Bourne et al., 2021***; ***World Health Organization, 2019***). Accurate characterization of visual function is critical for optimal intervention and patient support, but fraught with challenges. The gold clinical standard measure is visual acuity, the highest spatial resolution that can be discerned. This index mainly relies on a well-functioning fovea, the small retinal area with the highest density of photoreceptors, which processes the central 0°–2° around fixation. However, many forms of visual impairment do not affect the fovea alone. The vast majority of our visual input comes from peripheral vision, which provides coarse but invaluable information (***Alvarez, 2011***; ***Oliva, 2005***) – nearly all daily functions critically depend on intact functionality of the wider visual field, including driving, crossing the street, social function, mobility, and even reading (***Lange et al., 2021***). Accordingly, impairment of tissue beyond the fovea and its projections drastically affects function and quality of life (***Lange et al., 2021***; ***Lisboa et al., 2013***; ***Roh et al., 2018***; ***Subhi et al., 2017***). Still, testing visual function across the visual field remains limited in clinical and therapeutic contexts, especially in patients with drastic central vision loss. In this study, we aimed to address this gap by introducing a novel functional MRI (fMRI)-based approach to measure visual field sensitivity across a wide expanse of the visual field (40° diameter).

Beyond visual acuity, functional impairment across the wider visual field can be measured using a range of visual field tests, from the finger counting visual confrontation field test to more complicated and/or computerized tests (e.g., standard automatic perimetry, kinetic perimetry, microperimetry; ***Rai et al., 2024***). Computerized tests typically involve measuring sensitivity to the luminance contrast of a target relative to a background at different visual field locations while the participant's gaze is fixed on a central point. In some cases (e.g., microperimetry), sensitivity measurements are paired with fundus imaging, offering greater precision in linking visual field functions to specific retinal locations (***Rai et al., 2024***). As a result, visual field assessments can reveal functionally relevant deficits – including localized sensitivity loss and scotomas – that are not captured by foveal acuity alone, and are therefore potentially valuable for tracking disease progression and therapeutic efficacy.

Despite their clinical relevance, visual field testing comes with challenges and limitations, and as a result, the inclusion of visual field measures in sight-rescuing therapy trials is limited. First, it requires prolonged fixation and sustained visual attention. This can be very challenging for patients with severe vision loss, who often struggle to fixate, and strain to detect even high-intensity stimuli. This can lead to long and unpleasant testing sessions with unreliable results. Second, as perception of light stimuli is inherently subjective (***Rai et al., 2024***) and effortful, patients may vary in their criteria for visual recognition, and in their ability to report visual signals that are weakened or distorted by disease. Together, these constraints reduce the feasibility, robustness, and interpretability of conventional visual field testing in clinical trials, underscoring the need for alternative or complementary approaches that can assess functional vision while placing fewer demands on subjective reporting.

fMRI has recently been proposed as a promising alternative to measure visual field loss, as it requires no overt task, and instead measures visual sensitivity directly from brain responses (***Farahbakhsh et al., 2022***; ***Prabhakaran et al., 2021***; ***Ritter et al., 2019***). Population receptive field (pRF) mapping fMRI can measure which parts of the cortex respond to which parts of the visual scene (***Dumoulin and Wandell, 2008***). This is achieved by measuring local changes in cortical blood oxygenation in response to high-contrast stimuli such as flickering checkerboards that systematically traverse the visual field. These neural timeseries are then fit with a retinotopic spatial tuning function. The fMRI signal strength in a cortical region that encodes a specific visual field location provides information about visual sensitivity in this location (***Dumoulin and Wandell, 2008***). This approach has recently been used to accurately recover blind spots in the visual field detected with visual field perimetry (***Pawloff et al., 2023***; ***Ritter et al., 2019***). These results in turn suggest that fMRI may be a useful tool to monitor disease progression and recovery in visually impaired patients.

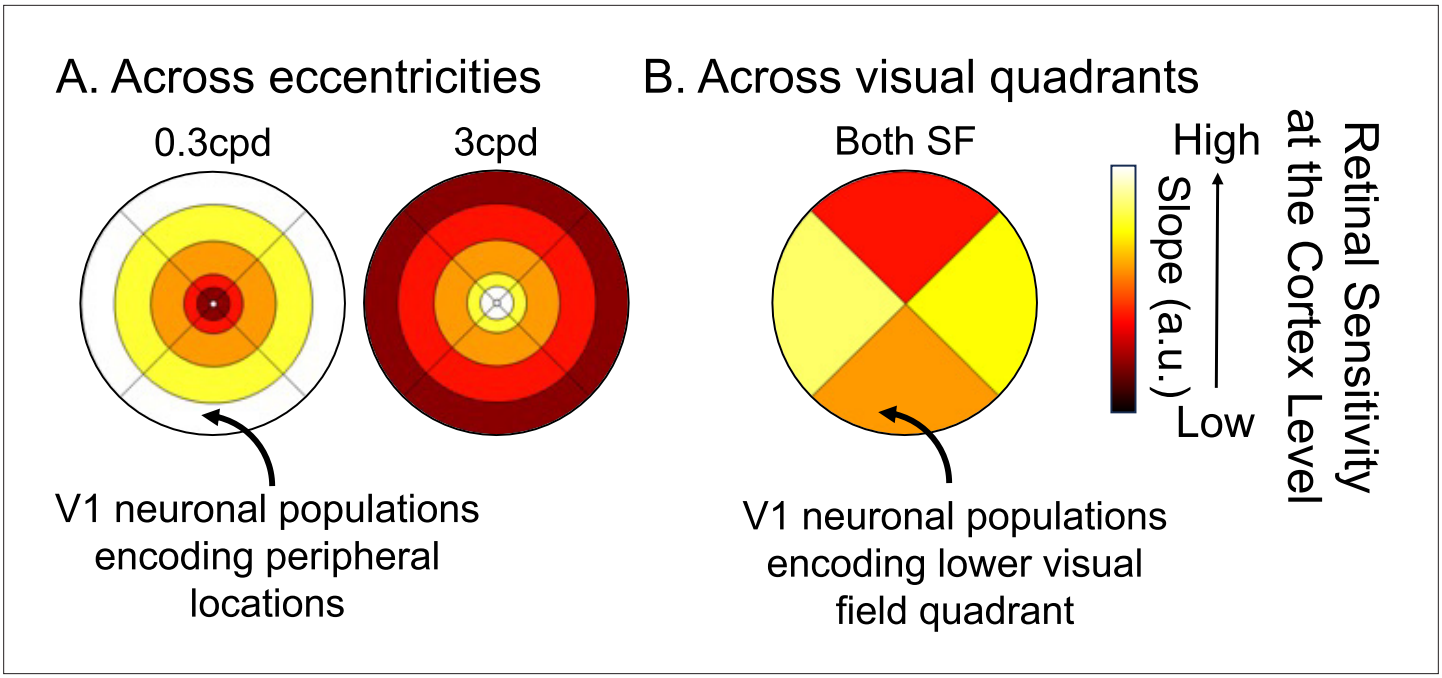


Figure 1. Expected changes in cortical contrast sensitivity in typically sighted controls for two different spatial frequencies (low spatial frequency, 0.3 cycles per degree (cpd), and high spatial frequency, 3.0 cpd), (**A**) as a function of eccentricity and (**B**) visual field quadrants. With reference to eccentricity, we expect higher sensitivity of V1 neuronal populations to (1) lower spatial frequencies in the periphery and (2) higher spatial frequencies in the center of the visual field. By comparison, we expect both high and low spatial frequency stimulation to evoke greatest sensitivity in V1 neuronal populations encoding the left and right visual quadrants, less in the lower, and least in the upper quadrant.

However, there are also significant challenges associated with this pRF mapping. Because pRF models require knowledge of where visual stimuli fall on the retina, this approach requires accurate and sustained fixation. If fixation is poor, the visual field locations assigned to cortical regions will be displaced, leading to noise or bias in the pRF maps. Additionally, most fMRI studies measure vision across a small central part of the visual fields (~10° of eccentricity), which will not capture critical dynamics in the periphery. Finally, most studies use a single maximum contrast stimulus to assess visual function (***Broderick et al., 2022***; ***Farahbakhsh et al., 2022***; ***Liu et al., 2006***; ***O'Connell et al., 2016***; ***Ritter et al., 2019***). This is suboptimal for at least two reasons: First, it may reduce the ability to detect subtle but clinically important changes that do not result in complete sensitivity loss or recovery. Second, with a single contrast stimulus, it becomes more difficult to determine whether a reduction in fMRI signal across sessions or brain regions reflects vision-related changes or other factors. Together, these factors currently limit the utility of neuroimaging-based visual field tests.

In this study, we sought to develop fMRI methods for measuring visual field sensitivity to address these challenges and to test its utility in artificial and realistic cases of visual field loss. Rather than presenting a single maximum contrast eccentricity-scaled checkerboard in a pRF mapping protocol, observers viewed large-field sinusoidal gratings at a range of contrasts without strict requirement to fixate. We used a large screen setup (40° diameter) to measure visual function across a large expanse of the visual field. To quantify visual sensitivity, we fit a simple cortical contrast response model to voxel timeseries evoked by the gratings, avoiding reliance on arbitrary signal amplitude thresholds. We first tested if this approach could sensitively and reliably quantify predicted contrast sensitivity differences across eccentricity and polar angle dimensions of the entire visual field (***Figure 1***), using a short, patient-friendly protocol in sighted controls. Critically, to achieve this, we linked cortical contrast sensitivity estimates to visual field locations using retinotopic tuning estimates obtained in a separate session. However, for patients with severe vision loss, it is infeasible to obtain accurate pRF measures due to poor ability to fixate a central target. We therefore also evaluated the approach using the structure-based atlas of retinotopic values developed by ***Benson et al., 2014***; ***Benson and Winawer, 2018***. This atlas predicts retinotopic organization by aligning individual cortical anatomy (e.g., surface curvature) to a group-average template that incorporates an algebraic model of retinotopy (***Benson***

et al., 2014). Once the subject's brain is aligned to this structural atlas, retinotopic maps defined by the model – that is, polar angle and eccentricity maps – are projected onto the individual's cortex. This allows estimation of visual field maps without requiring functional imaging, and provides a non-invasive, anatomy-driven approximation of visual field representations. To increase accuracy of the Benson atlas for our large-field stimuli, we subsequently fit these eccentricity estimates to the ***Horton and Hoyt, 1991*** model of cortical magnification in each individual.

We demonstrate that our approach can recover, at a cortical level, known sensitivity changes across the visual field. V1 neuronal populations encoding the central visual field show the highest sensitivity to high spatial frequencies, while those encoding the periphery are most sensitive to low spatial frequencies. We also find greater sensitivity in V1 regions receiving visual inputs from the horizontal compared to vertical quadrants, and from the lower compared to upper quadrants. Crucially, these effects are detectable at the individual level and repeatable across visits, suggesting our approach will be suitable for detecting visual field sensitivity changes over time (e.g., due to learning, aging, disease progression, or recovery). Moreover, when using the Benson atlas instead of individual pRF measures to link neuronal responses to visual field locations, we still detect these effects, although with slightly reduced sensitivity. We also demonstrate the clinical relevance of this approach by recovering simulated scotomas (i.e., a ring of visual field loss around fixation and the loss of an entire visual field quadrant), as well as visual field loss in a patient with a neurodegenerative disorder causing large areas of visual field loss. We conclude that this approach, that is, the combination of cortical contrast sensitivity testing, large field stimulation, and a large-field calibrated retinotopic atlas, may be particularly useful for quantifying visual recovery in patients, whether spontaneous or following gene-therapy interventions, and for linking brain-based activations to behavioral performance.

Results

To measure visual field function, we developed a new measure of cortical contrast sensitivity, assessing the brain's ability to discriminate gratings of varying spatial frequencies based on luminance variations. This depends on many factors, including the size, orientation, and density of cells in different parts of the retina. As these factors change across the visual field, contrast sensitivity varies with spatial frequency and visual field location in the typical, healthy visual system. We first investigated whether our brain-based approach can reliably detect these known differences in contrast sensitivity as a function of eccentricities (up to 20° from fixation) and visual field quadrants, in individual normal-sighted controls. We then investigated whether our approach could recover loss of visual inputs at the cortical level, either simulated in a healthy control or pathological in a patient. In each section, findings were first reported for the pRF-defined ROIs and then for the Benson-defined ROIs.

Spatial frequency preference changes in V1 neuronal populations across eccentricities

For high spatial frequency stimuli, we expected better sensitivity in V1 neuronal populations encoding central locations in visual space than in those encoding the periphery. In contrast, for low spatial frequency information, we expected the opposite, better sensitivity in V1 neuronal populations encoding the periphery than the center of the visual field.

Using ANOVA, we found the expected interaction between spatial frequency and eccentricity ($F(1.96, 11.79) = 28.66$, $p < 0.001$; ***Figure 2***) as well as a main effect of eccentricity ($F(2.33, 13.99) = 12.67$, $p < 0.001$). These effects were statistically significant at the individual participant level showing high sensitivity (***Figure 2A***, transparent lines show individual data; ***Figure 2C*** shows individual visual field plots; for stats, see ***Appendix 1—table 1***).

Post hoc tests using Holm–Bonferroni correction show that V1 neuronal populations receiving inputs from the central visual field (0.5°–4.5°) showed greater contrast sensitivity to high spatial frequency as compared to low spatial frequency stimuli (steeper slope for the 3 versus 0.3 cpd condition: **0.5°–2.5°**: $t(6) = 4.35$, $p_{bonf} = 0.0149$; **2.5°–4.5°**: $t(6) = 3.471$, $p_{bonf} = 0.0266$). Conversely, peripheral eccentricities in V1 (above 9.5°) showed higher contrast sensitivity to low as compared to high spatial frequency stimuli (steeper slope for 0.3 versus 3 cpd condition: **9.5°–15°**: $t(6) = -4.591$, $p_{bonf} = 0.0149$; **15°–20°**: $t(6) = -6.615$, $p_{bonf} = 0.0029$). Between 4.5° and 9.5°, V1 contrast sensitivity was similar for both spatial frequencies ($t(6) = -0.226$, $p_{bonf} = 0.8286$). Crucially, these effects remained when using retinotopic

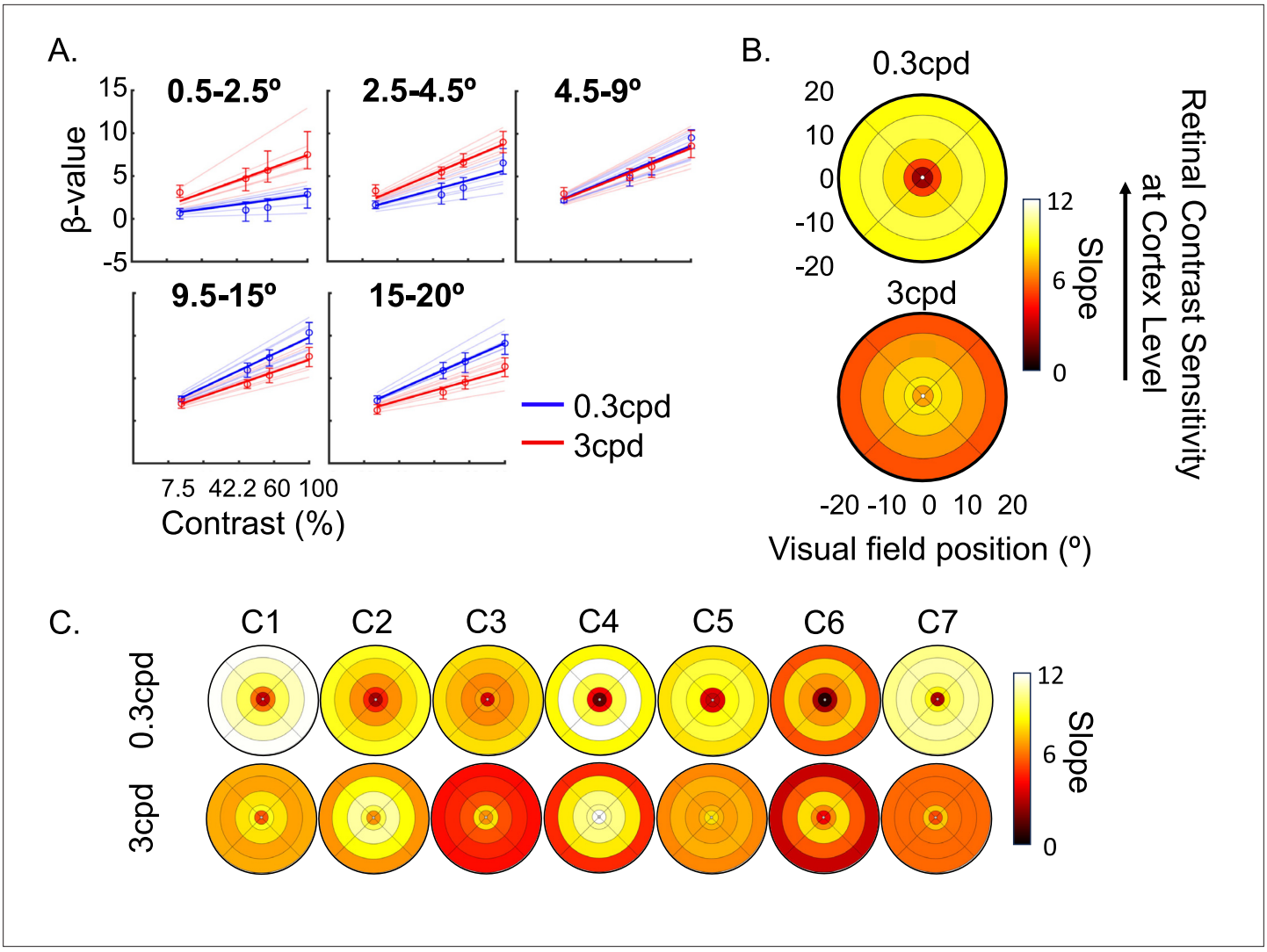


Figure 2. Spatial frequency preference V1 across the visual field. For each participant (n = 7), five eccentricity bins were defined using subject-specific pRF estimates: 0.5°–2.5°, 2.5°–4.5°, 4.5°–9.5°, 9.5°–15°, and 15°–20°. (**A**) Average β-values versus stimulus contrasts for low (0.3 cpd; blue) and high (3 cpd; red) spatial frequencies across eccentricity bins. Error bars are the 95% confidence intervals. Thick lines represent the group-level model fit (n=7), thin lines are the individual fits. (**B**) Slopes projected into visual space for low (0.3 cpd) and high (3 cpd) spatial frequencies. The color scale corresponds to slope estimates, with higher values indicating higher cortical contrast sensitivities. (**C**) Heat plots for each participant (**C1–C7**).

estimates based on structural scans derived from the Benson retinotopic atlas instead of the pRF-mapping measures (**0.5°–2.5°**: $t(6) = 5.768$, $p_{bonf} = 0.0059$; **2.5°–4.5°**: $t(6) = 2.531$, $p_{bonf} = 0.0892$; **4.5°–9.5°**:$t(6) = -0.293$, $p_{bonf} = 0.7792$;**9.5°–15°**:$t(6) = -3.274$, $p_{bonf} = 0.0509$;**15°–20°**:$t(6) = -3.528$, $p_{bonf} = 0.0496$; see ***Appendix 1—figure 2*** and ***Appendix 1—table 3***).

These results demonstrate that our approach can detect subtle changes in visual sensitivity across eccentricities at the individual participant level. The ability to reveal these gradients was made possible by the large peripheral coverage provided by our large-field stimulation setup (see ***Appendix 1—figure 1***), which enabled a more complete characterization of V1 sensitivity across the visual field. Importantly, the same effects were preserved when using retinotopic estimates derived from structure-based atlases, demonstrating that atlas-based methods can be used as alternatives to pRF mapping in cases where it might otherwise be difficult or impossible to directly collect pRF measures. Together, these highlight both the validity of our approach and its potential to broaden the scope of visual neuroscience.

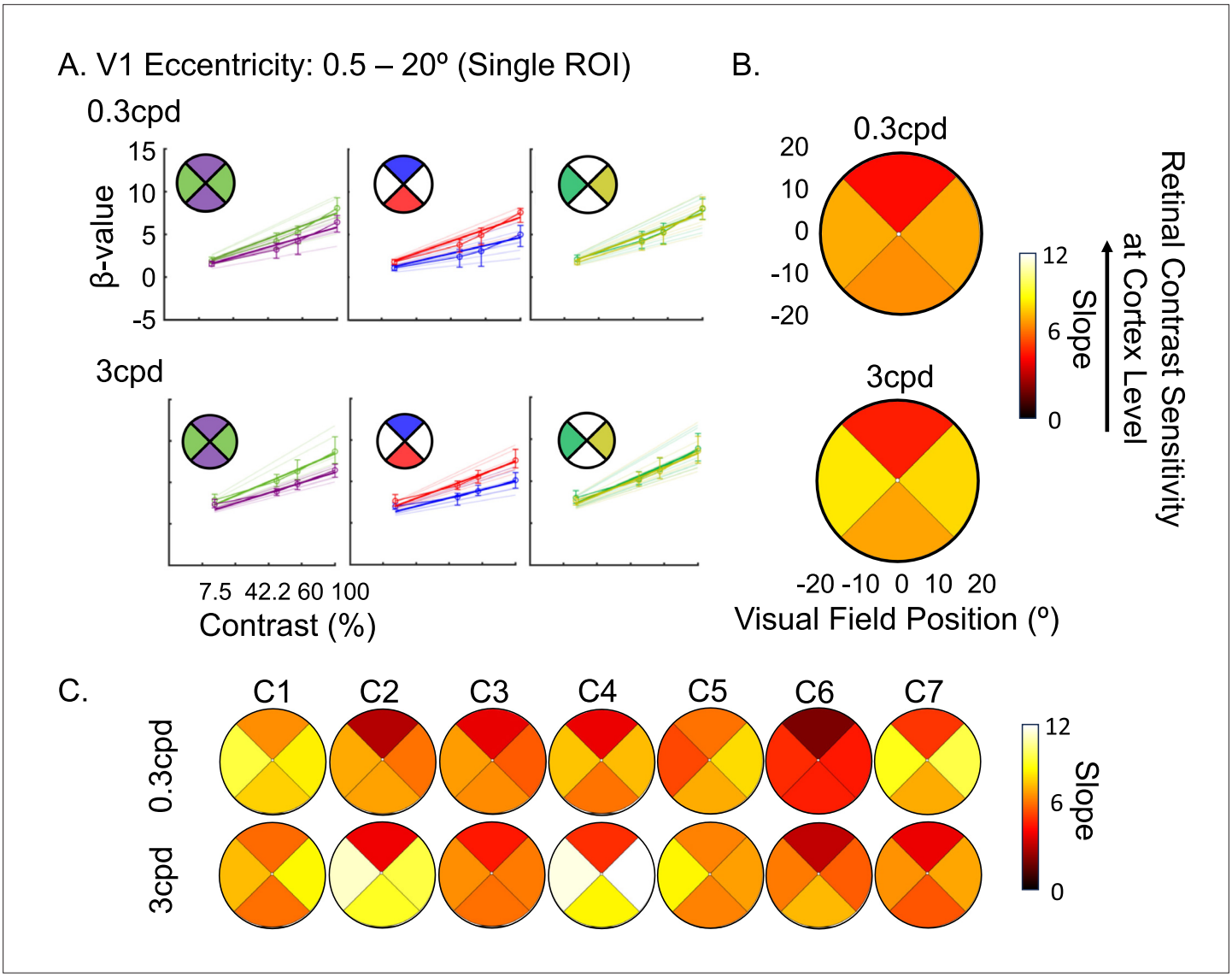


Figure 3. Anisotropies in V1 across visual field quadrants for low (0.3 cpd; top row) and high (3 cpd; bottom row) spatial frequencies. For each participant (n=7), pRF estimates were used to link brain responses to visual field positions. Visual quadrants are ±45° around the cardinal meridians, with slope values for eccentricities between 0.5° and 20°. Horizontal quadrants are left and right; vertical quadrants are upper and lower. (**A**) Average β-values versus contrast levels for each anisotropy (horizontal versus vertical, upper versus lower, left versus right). Error bars are 95% confidence intervals. Thick lines correspond to group-level model fit, while thin lines are individual fits. (**B**) Slope values projected onto visual field quadrants. The color scale represents slope estimates, with higher values indicating greater V1 contrast sensitivity. (**C**) Heat plots for each participant (**C1–C7**).

Contrast sensitivity is not equal across the visual field quadrants in V1 neurons

Contrast sensitivity is known to vary across the quadrants of the visual field; previous behavioral studies have shown greater contrast sensitivity along the horizontal versus vertical meridians, and along the lower versus upper vertical meridian (***Barbot et al., 2021***; ***Carrasco et al., 2022***; ***Himmelberg et al., 2020***; ***Himmelberg et al., 2023***). Recent fMRI studies have also shown that these asymmetries in BOLD response amplitude to single contrast gratings (***Kurzawski et al., 2022***; ***Liu et al., 2006***; ***O'Connell et al., 2016***). Therefore, we expect our fMRI approach to uncover these established asymmetry patterns at the cortical level.

Figure 3 shows how cortical contrast sensitivity in V1 varies across visual field quadrants, for the 0.3 and 3 cpd conditions. For this analysis, we collapsed eccentricities (0.5°–20°) into a single bin. We found a main effect of visual field quadrant location on V1 sensitivity ($F(2.46, 14.76) = 20.71,\ p < 0.001$). Post

hoc pairwise comparisons using Holm–Bonferroni corrections revealed that, as predicted, the cortical contrast response function had a higher slope – indicating better V1 sensitivity – along the horizontal versus vertical quadrants (Horizontal–Vertical Anisotropy – **HVA:** $t(6) = 5.908,\ p_{bonf} = 0.0031$) and along the lower versus upper quadrant (Vertical Meridian Anisotropy – **VMA:** $t(6) = 4.106,\ p_{bonf} = 0.0126$). Conversely, no difference in cortical contrast sensitivity was found between V1 neuronal populations encoding the left and right quadrants of the visual field (Left–Right Horizontal Meridian Anisotropy – **LRHMA:** $t(6) = 0.7197,\ p_{bonf} = 0.4988$). Moreover, there was no interaction between spatial frequency and visual field quadrant positions ($F(2.16, 12.99) = 1.34,\ \mathrm{p} = 0.298$), suggesting V1 visual field anisotropies are relatively constant across spatial frequencies. Importantly, all these differences are also present in individual participants (***Figure 3A***, transparent lines are individual data, ***Figure 3C*** shows individual visual field plots; for stats, see ***Appendix 1—table 2***). All participants had better V1 sensitivity in the horizontal versus vertical quadrants. Six out of seven participants showed asymmetries between the lower and upper quadrants. Differences in V1 sensitivity between left and right quadrants were inconsistent across participants (three participants: left > right; two participants: right > left; two participants: non-significant), in line with no difference at the group level. This again demonstrates the high sensitivity of our approach for identifying and quantifying sensitivity changes across the visual field, at the individual participant level, offering a potential valuable tool for assessing and addressing visual field loss in clinical populations.

We next tested if we could recover these V1 anisotropies when using retinotopic estimates based on structural scans fit with the Benson atlas instead of pRF measures (see ***Appendix 1—figure 3*** and ***Appendix 1—Tables 3 and 4***). We found that the horizontal–vertical anisotropy effect was recovered (**HVA:** $t(6) = 3.584,\ p_{bonf} = 0.0347$), but that the vertical meridian anisotropy effect was not (**VMA:** $t(6) = 0.744,\ p_{bonf} = 0.9697$) with this approach. These results provide evidence that our approach can still detect subtle visual field quadrant anisotropies using a structure-based retinotopic atlas, although less accurately.

While the most pronounced contrast sensitivity difference along visual field quadrants (horizontal versus vertical quadrants) was retained when the adjusted Benson atlas was used to replace pRF measurements, not all anisotropies survived. This may be because the template does not model cortical magnification differences along meridians, reducing accuracy. It is not surprising that retinotopic estimates based on structure-retinotopy relationship modeling provide less accurate estimates of retinotopic tuning of neuron populations in V1 than direct measures of the individual retinotopy. Any individual deviations from the model make it more challenging to accurately assign cortical contrast sensitivity to visual field locations, potentially decreasing the ability to detect changes in visual function across the field. Given this challenge, results with the adjusted Benson map are surprisingly similar to those based on pRF measurement, showing promise for clinical applications when pRF mapping is unfeasible.

V1 sensitivity differences across the visual field are reproducible across visits

Having shown that changes in cortical contrast sensitivity across the visual space can be detected with fMRI, it is crucial to determine how reliable our measure is. This is especially important for potential applications in monitoring changes over time. Using Spearman correlations, we measured the reliability of cortical contrast sensitivity estimates for the 0.3 cpd spatial frequency condition across two repeated measurements, collected on two different days. We collected test–retest reliability measures from four out of seven participants (***Figure 4A, B***) and benchmarked them against the correlations between the 0.3 cpd condition and 3 cpd spatial frequency condition, collected in the same session (***Figure 4C***). If measures are reliable, correlations should be higher for repeated measures with the same spatial frequency stimulus, collected on different days. We tested this prediction using a one-tailed paired *t*-test.

Our findings clearly show that the gradual increase in cortical sensitivity toward the periphery for the 0.3 cpd condition is consistent across the two sessions (***Figure 4A***). Moreover, the data of individual participants show characteristic profiles that stay highly consistent. Additionally, we observed moderate-to-strong positive Spearman correlations across sessions for the 0.3 cpd condition (***Figure 4B***; **C2**: $\rho = 0.5793$; **C4**: $\rho = 0.6996$; **C5**: $\rho = 0.4059$; **C6**: $\rho = 0.7677$), which were consistently higher than those across different spatial frequency conditions (***Figure 4C***; **C2**: $\rho = 0.5503$; **C4**: $\rho = 0.2318$; **C5**:

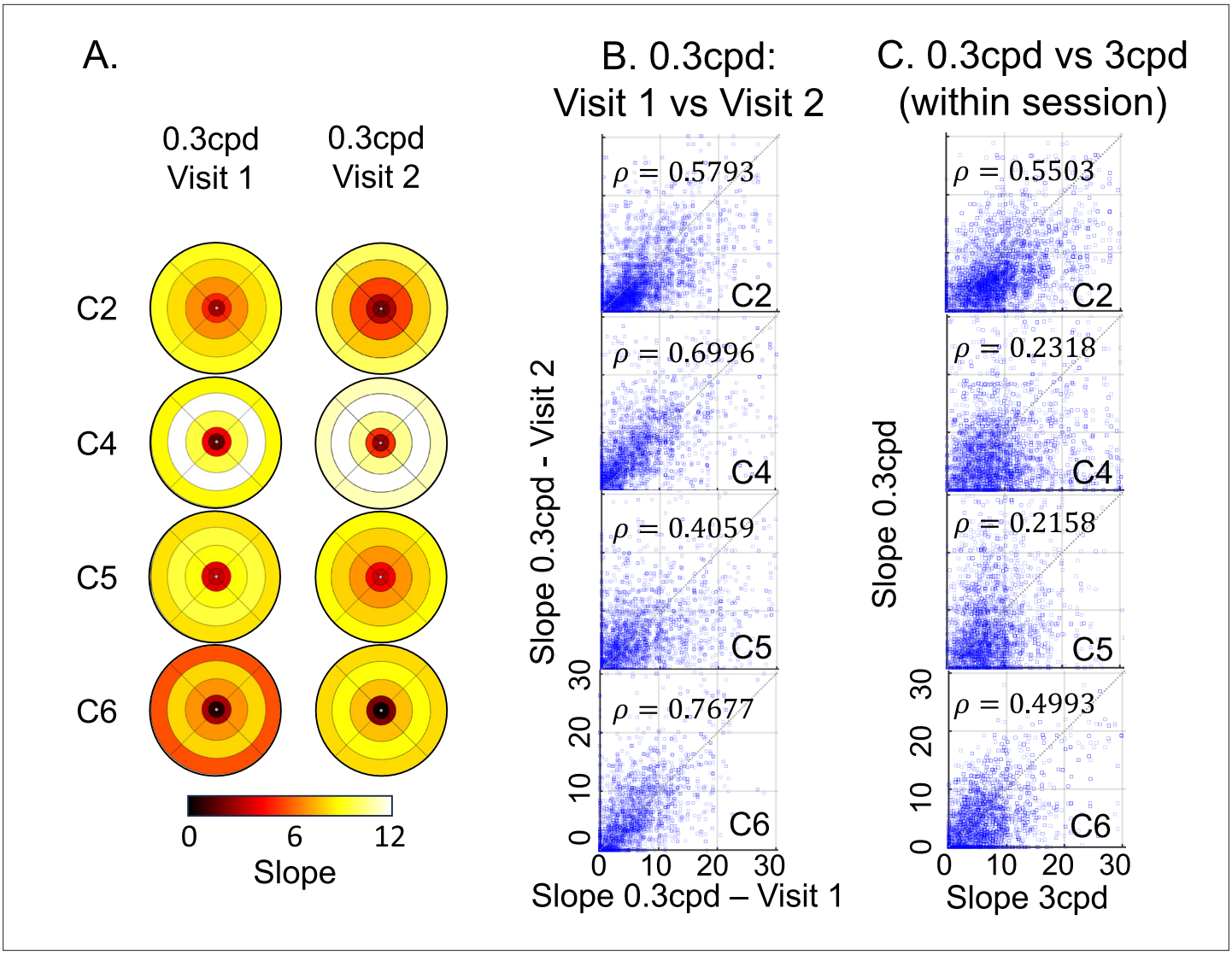


Figure 4. Reliability of V1 slopes across sessions, in four of the seven controls. (**A**) V1 contrast sensitivity (i.e., slopes) plotted in visual field space (using pRF estimates), showing a consistent session-independent increase in cortical sensitivity toward peripheral locations for the 0.3 cpd condition. Higher slopes (warmer colors) indicate higher V1 sensitivity. (**B**) Slopes for the 0.3 cpd condition across two visits. Spearman correlation coefficients (ρ) between visits are shown on the figure. (**C**) Slopes for the 0.3 and 3 cpd conditions collected within the same session. Spearman correlation coefficients (ρ) between visits are shown on the figure.

$\rho = 0.2158$; **C6**: $\rho = 0.4993$). This difference was statistically significant ($t(3) = 2.62$, $p < 0.0395$). This indicates that within participants, our measure is reliable across sessions and distinguishes effectively between patterns elicited by various spatial frequency conditions. Collectively, this suggests that our measure could serve as a robust tool for detecting changes in cortical sensitivity, such as those occurring over time or following therapeutic interventions.

Effect of eye movements on V1 cortical sensitivity

So far, we have demonstrated that our measure of cortical sensitivity can reliably recover known gradients in sensitivity across eccentricities and visual quadrants. We also showed that this measure was consistent across visits and sessions, suggesting its potential utility for monitoring changes over time. However, all prior tasks were conducted under conditions of central fixation, with participants instructed to maintain gaze on a central dot. A key motivation for this approach was its theoretical robustness to fixation instability. We therefore also aimed to investigate how varying degrees of eye movement might influence cortical sensitivity across the visual field.

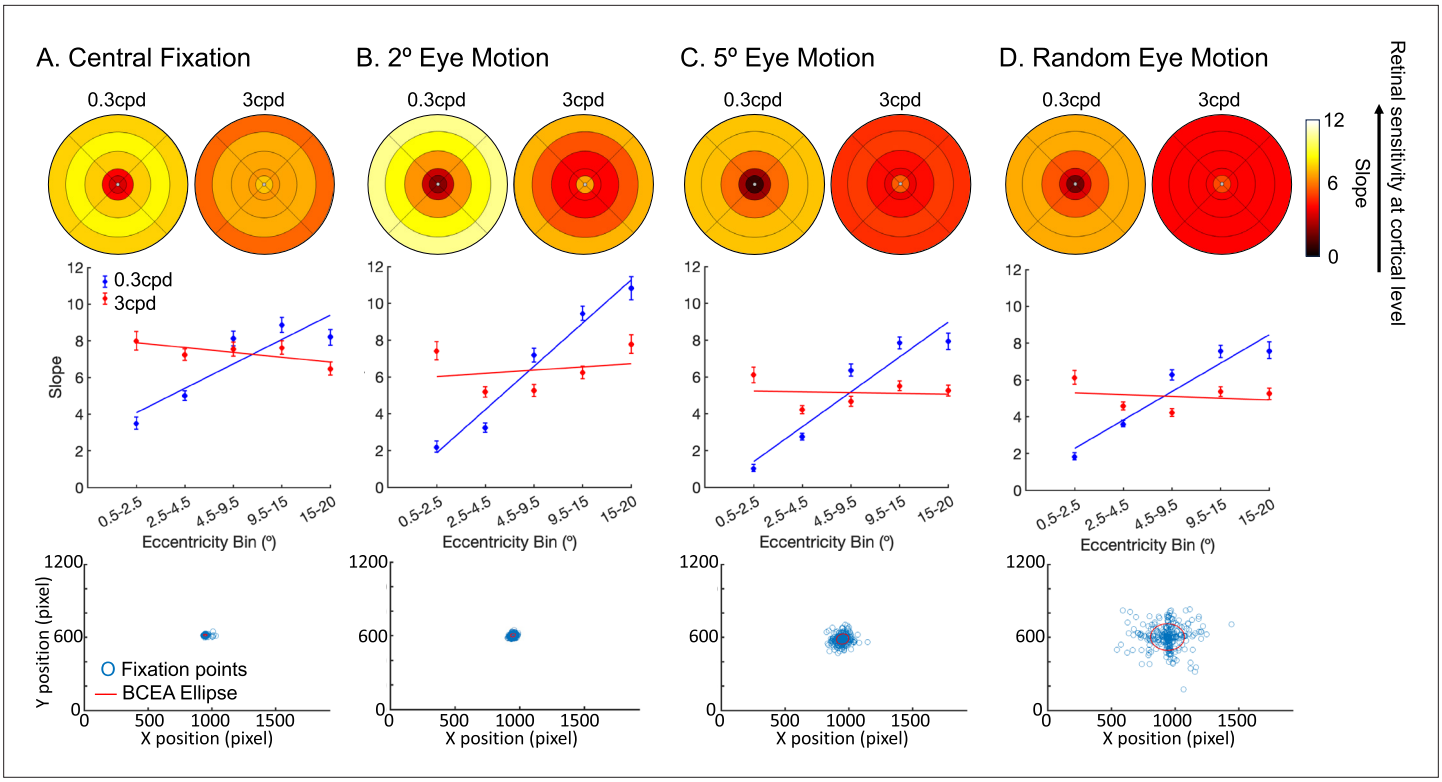


Figure 5. Effect of eye movements on slope estimation, in participant C5. Each column represents a distinct eye movement condition: (**A**) central fixation, (**B**) 2° eye motion, (**C**) 5° eye motion, and (**D**) random eye motion. pRF estimates were used to relate brain responses to visual field positions. **Top row:** Heatmaps of slope distributions for low (0.3 cycles per degree, cpd) and high (3 cpd) spatial frequency stimuli, with warmer colors indicating steeper slopes. **Middle row:** Slope values scattered across eccentricity bins (0.5°–2.5°, 2.5°–4.5°, 4.5°–9.5°, 9.5°–15°, and 15°–20°), illustrating how cortical sensitivity varies across the visual field for low (blue) and high (red) spatial frequencies. Error bars represent 95% confidence interval. **Bottom row:** Fixation stability plots from one out of three runs, including fixation points (blue) and BCEA ellipses (red). BCEA values quantify gaze dispersion: Central Fixation (0.91 deg^2), 2° eye motion (2.43 deg^2), 5° eye motion (18.41 deg^2), and random eye motion (130.79 deg^2). Despite increased eye movements and reduced slope values – particularly for high spatial frequency stimuli – the overall pattern of cortical sensitivity remains consistent across conditions.

To address this, two participants (C5 and C6) completed a modified version of the contrast sensitivity task in which they made eye movements either by following a dot moving randomly at a radius of 2° or 5° around fixation, or by self-initiated very large eye movements. Eye movements across these conditions (***Figure 5***, bottom row; ***Figure 6***, bottom row) were quantified using bivariate contour ellipse area (BCEA; **C5** – central fixation: mean ± SD = 0.57 ± 0.11 deg^2, 2° eye motion: 2.69 ± 0.48 deg^2, 5° eye motion: 20.3 ± 1.32 deg^2, random eye motion: 133.7 ± 23.36 deg^2; **C6** – central fixation: 0.96 ± 0.56 deg^2, 2° eye motion: 1.28 ± 0.15 deg^2). For reference, in severe (idiopathic) nystagmus, the eye movement variability along the vertical and horizontal planes is 1.08 and 1.60 deg, respectively (***Tailor et al., 2021***). Assuming a moderate correlation between axes ($\rho = 0.3$), the average fixation stability would equate to a BCEA of ~21.46 deg^2 (i.e.,~5° eye motion condition in our data).

Despite these very large levels of eye movements, we observed that the overall cortical contrast sensitivity spatial pattern across eccentricity remained remarkably consistent (***Figure 5***, top and middle rows; ***Figure 6***, top row). However, at the most extreme movements, contrast sensitivity estimates (slope values) were lower; and while the overall cortical visual field map structure was still clearly present for low spatial frequencies, it appeared more flattened for 3 cpd, suggesting reduced sensitivity of our measure for large eye movement and high spatial frequency stimuli.

A test-case of simulated loss of visual inputs

In the previous sections, we showed that the slope of a square root function provides a reliable measure of contrast sensitivity in the brain of healthy controls. But can this brain-level model also quantify loss of visual inputs? To test this, we first simulated an artificial scotoma in one normally sighted participant, by (a) masking a region of the visual field with a gray, annular ring, covering 3°–8°

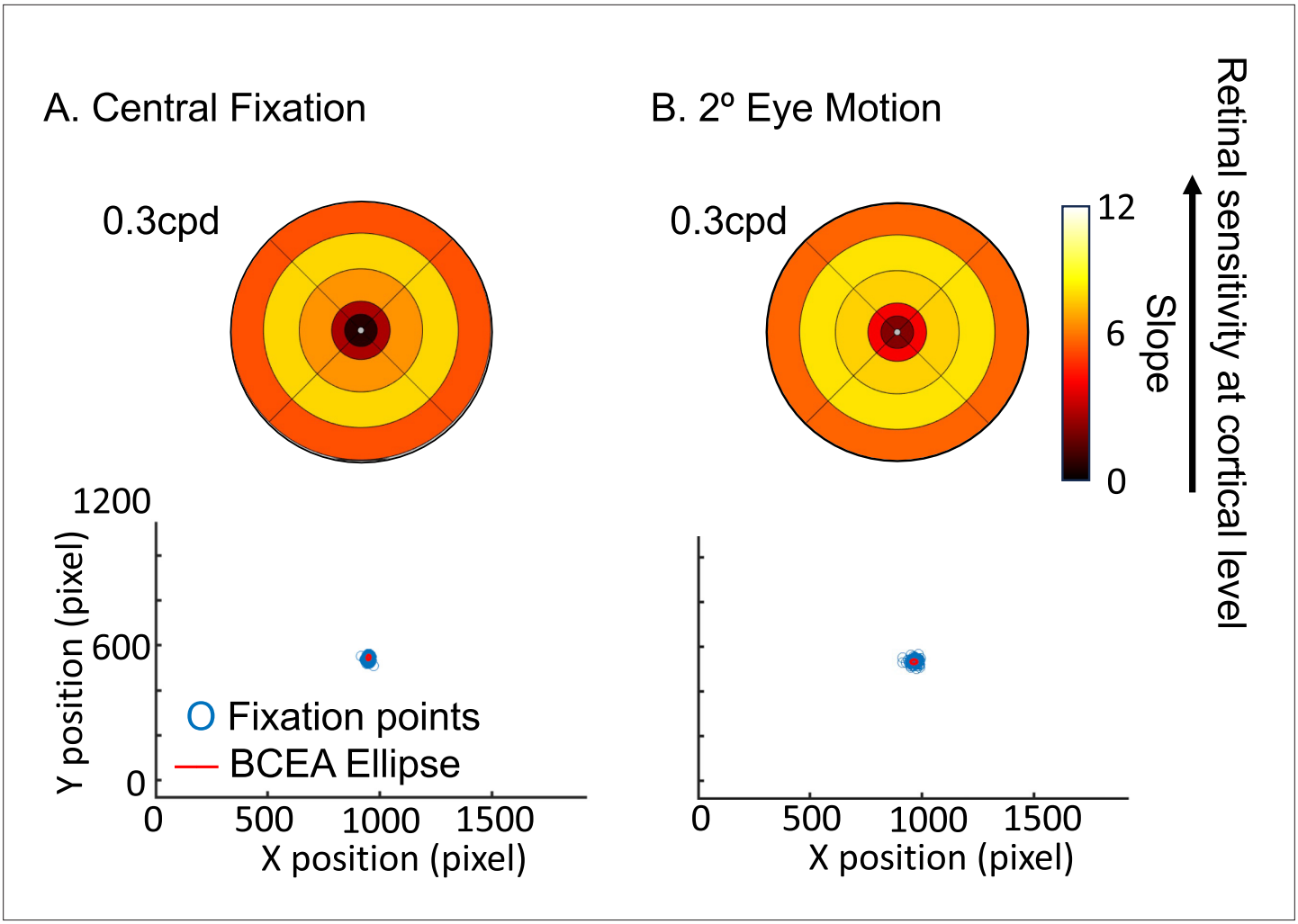


Figure 6. Effect of eye movements on slope estimation, in participant C6. Each column represents a distinct eye movement condition: (**A**) central fixation and (**B**) 2° eye motion. pRF estimates were used to relate brain responses to visual field positions. **Top row:** Heatmaps of slope distributions for low (0.3 cycles per degree, cpd) and high (3 cpd) spatial frequency stimuli, with warmer colors indicating steeper slopes. **Bottom row:** Fixation stability plots from one out of 3 runs, including fixation points (blue) and BCEA ellipses (red). BCEA values quantify gaze dispersion: Central Fixation (0.76 deg^2) and 2° eye motion (1.23 deg^2).

eccentricity (***Figure 7A***), and (b) masking the upper-right visual quadrant using a gray quarter-sector overlay (***Figure 8A***). We expect smaller slope values in V1 neuronal populations that would under normal circumstances encode that part of the visual space.

As expected, we observed reduced responses in V1 locations corresponding to the artificial scotoma (***Figures 7 and 8***), with increased responses along the edges of the mask for the ring scotoma condition (***Figure 7***). This artificial loss of visual input was also clearly present in the cortical contrast sensitivity estimate, with significantly reduced slope steepness in V1 between 3° and 8° for the ring scotoma condition (***Figure 7C, D***) and in the upper-right quadrant for the quarter-sector scotoma condition (***Figure 8B, C***). Additionally, we could recover this scotoma using the calibrated Benson template, although less accurately (***Figures 7E and 8D***). These results show that this measure of V1 contrast sensitivity is sensitive enough to detect loss of visual inputs in the brain at an individual level, when a complete local loss of sight is simulated, and that this approach does not crucially rely on pRF mapping data from the individual. This supports the utility of our approach in recovering patterns of vision loss and recovery at a cortical level.

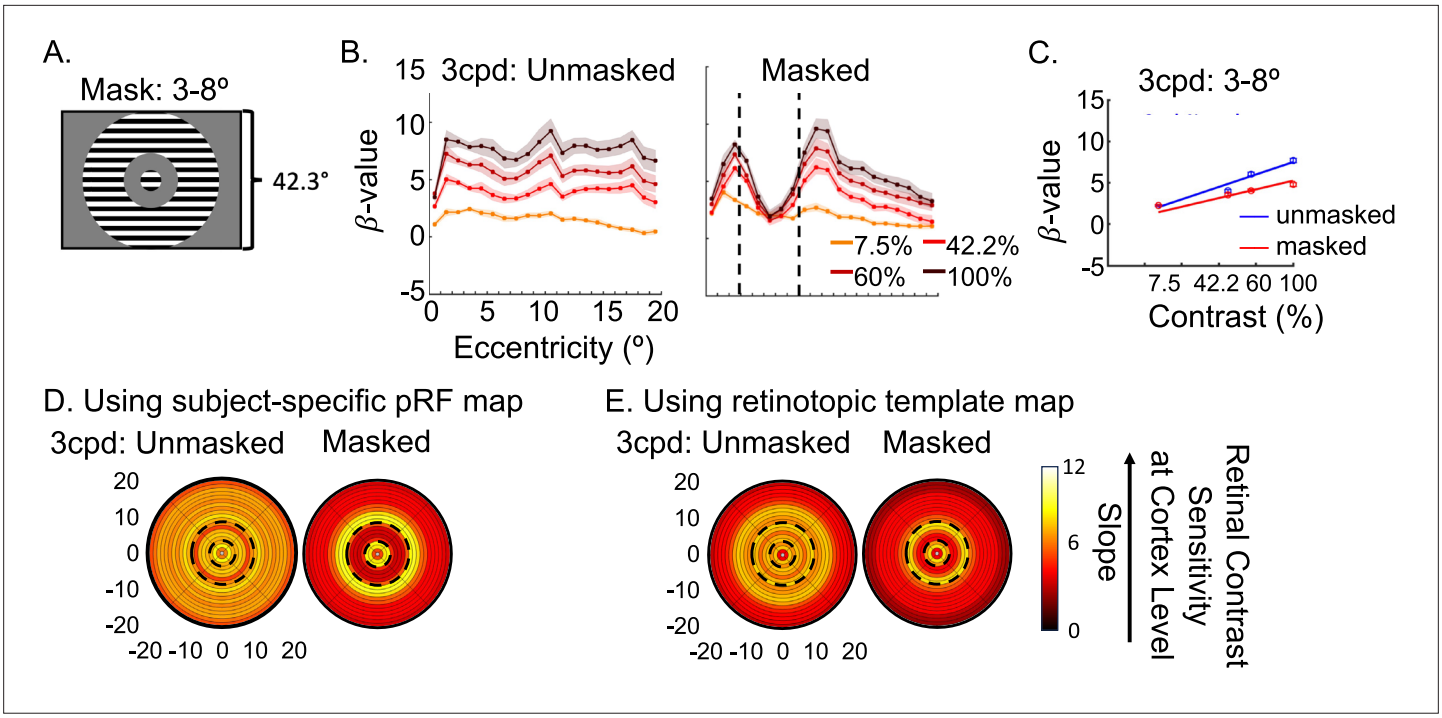


Figure 7. V1 sensitivity (i.e., slope) to 3 cpd condition, in the region of the artificial scotoma (3°–8°) in participant C5. (**A**) Masked region between 3° and 8°, representing the artificial scotoma. (**B**) Averaged β-values between 0.5° and 20° eccentricities in V1, under normal and masked conditions. 20 eccentricity bins of 1° were selected based on pRF estimates. The color scale indicates the presented contrast levels, and the black dotted lines mark the boundaries of the artificial scotoma. Shaded area represents 95% confidence interval. (**C**) Average β-values versus contrast levels in V1 neurons encoding the region of artificial scotoma (3°–8°), under normal (blue) and masked (red) conditions. Lines correspond to the model fitted to the data. Error bars (masked by dots) represent 95% confidence interval. (**D**) Slopes projected back onto the visual field under normal and masked conditions. pRF estimates were used to relate brain responses to visual field locations and to create the 1° eccentricity bins. The boundaries of the simulated scotoma region are represented by dotted lines. The color scale indicates slope estimates, with higher values (warmer colors) corresponding to higher V1 contrast sensitivity. (**E**) Slopes plotted back into the visual space using the calibrated Benson template instead of pRF estimates.

Case of severe central vision loss

We next tested if brain-based cortical contrast sensitivity could recover visual field loss in a clinical patient with Leber Hereditary Optic Neuropathy (LHON; M, 45.5 years old, mutation: m.11778G>A, disease duration: 36.1 years). LHON is a neurodegenerative disease caused by mitochondrial DNA mutations, leading to acute loss of retinal ganglion cells across large visual field areas. LHON patients often present with dense, central scotoma extending up to 10°–15° around fixation.

As vision loss often varies between eyes, the patient underwent monocular testing for the fMRI contrast sensitivity task (tested spatial frequencies: 0.3 and 1 cpd). For comparison, a behavioral visual field perimetry map was obtained with the Compass fundus perimeter (CenterVue, Padova, Italy) for each eye, using a 24-2 testing grid with a Goldmann size III target (54 locations: 52 from the 24-2 grid, 1 at fixation, and 1 at the physiological blind spot). The Compass actively tracks the retina to compensate for fixation loss, automatically repositioning targets based on current eye position. Sensitivity thresholds at each location were determined using the ZEST projection strategy implemented in the device. The patient, who had some preserved central vision, could see the fixation targets in behavioral testing and the scanner, making them an ideal participant for methods evaluation.

The Compass perimetry map revealed drastic loss of sensitivity across the visual field (***Figure 9*** – top row). For the left eye, the left hemifield was more affected than the right, with most severe loss in the upper-left quadrant. In contrast, the right eye showed more reduced sensitivity in the right hemifield, particularly in the upper-right quadrant.

We found correspondence between affected and non-affected visual field regions across the Compass and the fMRI contrast sensitivity measures (***Figure 9***). Here, V1 contrast sensitivity (i.e., slope values) was computed for the upper-left, upper-right, lower-left, and lower-right quadrants to match the layout from the Compass visual field maps. Using the brain-based approach, we recovered

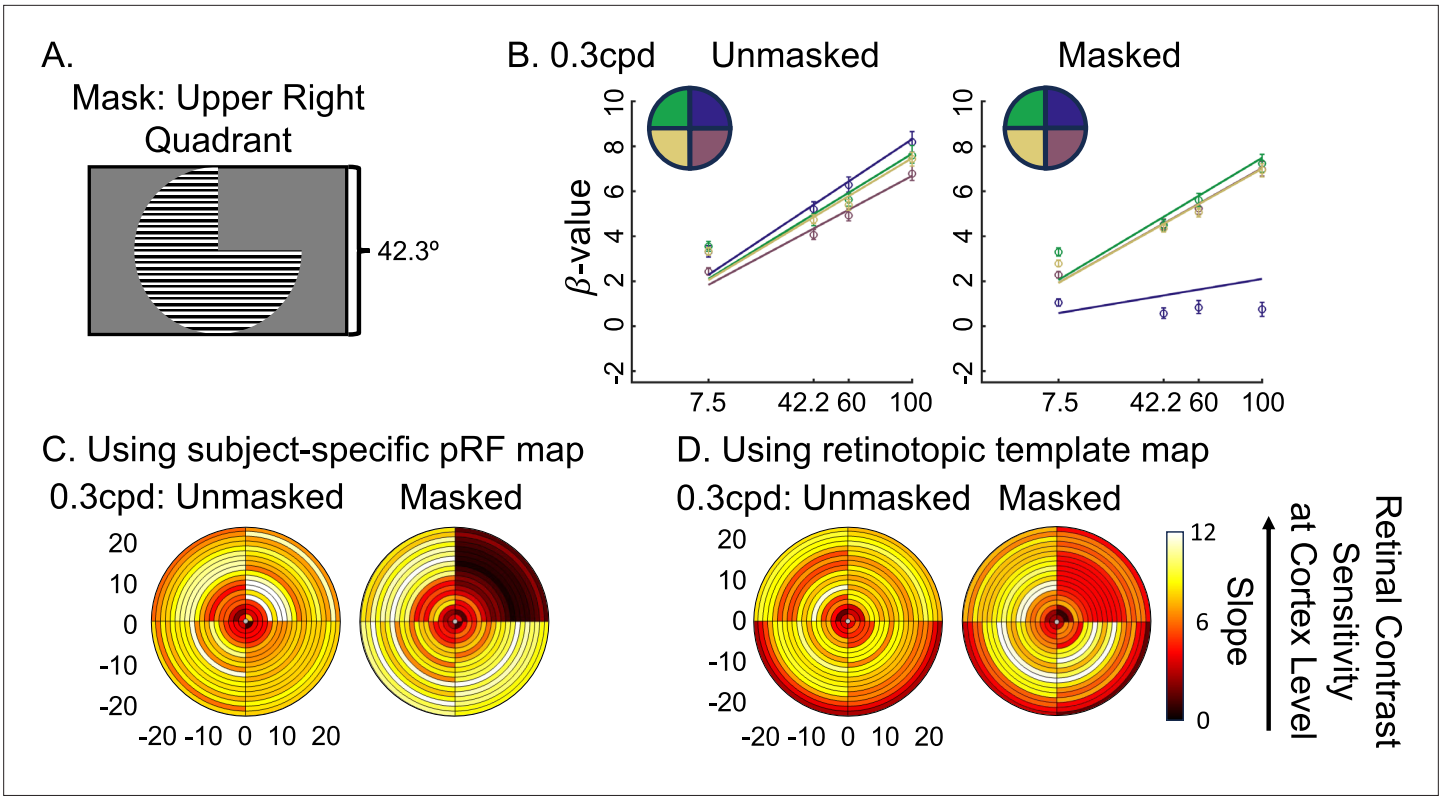


Figure 8. V1 sensitivity (i.e., slope) to 0.3 cpd condition, in the region of the artificial scotoma (upper right quadrant) in participant C5. (**A**) Masked upper right quadrant region, representing the artificial scotoma. (**B**) Average β-values versus contrast levels in V1 neurons encoding each of the four quadrants: upper left (yellow), upper right (cyan), bottom left (red), and bottom right (blue). Lines correspond to the model fitted to the data. Error bars represent 95% confidence interval. (**C**) Slopes projected back onto the visual field under normal and masked conditions. pRF estimates were used to relate brain responses to visual field locations and to create the 1° eccentricity bins. The color scale indicates slope estimates, with higher values (warmer colors) corresponding to higher V1 contrast sensitivity. (**D**) Slopes plotted back into the visual space using the calibrated Benson template instead of pRF estimates.

sensitivity loss in the upper-right visual quadrant for the right eye at the cortical level, reflected in smaller cortical contrast sensitivity slopes in V1 neuronal populations encoding that area. For the left eye, cortical contrast sensitivity was also lower in the upper-left quadrant of the visual field, but differences were less pronounced. This is in line with the observation that the left eye was the better eye, with substantially less severe vision loss in the affected regions (lighter shading, ***Figure 9*** – top row). When using the calibrated Benson atlas instead of pRF mapping data to link neuronal responses to visual locations, this pattern was retained for the right eye, but the more subtle pattern in the left eye became noisier.

By combining large-field stimulation and contrast sensitivity modeling in fMRI, with the cortical magnification-adjusted Benson atlas, these data show how brain-based measures could provide a tool to characterize vision loss in patients without need for demanding tasks or sustained precise fixation, while highlighting challenges of detecting more subtle vision loss and pinpointing it to visual locations.

Discussion

In this study, we aimed to develop and validate an fMRI-based method for measuring cortical contrast sensitivity across a broad extent of the visual field in V1, addressing the limitations of traditional visual field tests and existing neuroimaging approaches. To achieve this, we implemented a large-field presentation setup in fMRI, allowing us to stimulate the visual cortex up to 20° eccentricity. By integrating population receptive field (pRF) modeling with contrast sensitivity measurements of the BOLD response to large-field sinusoidal gratings varying in contrast levels and spatial frequencies, we created a quantitative, sensitive, and reliable measure of cortical contrast sensitivity. Our

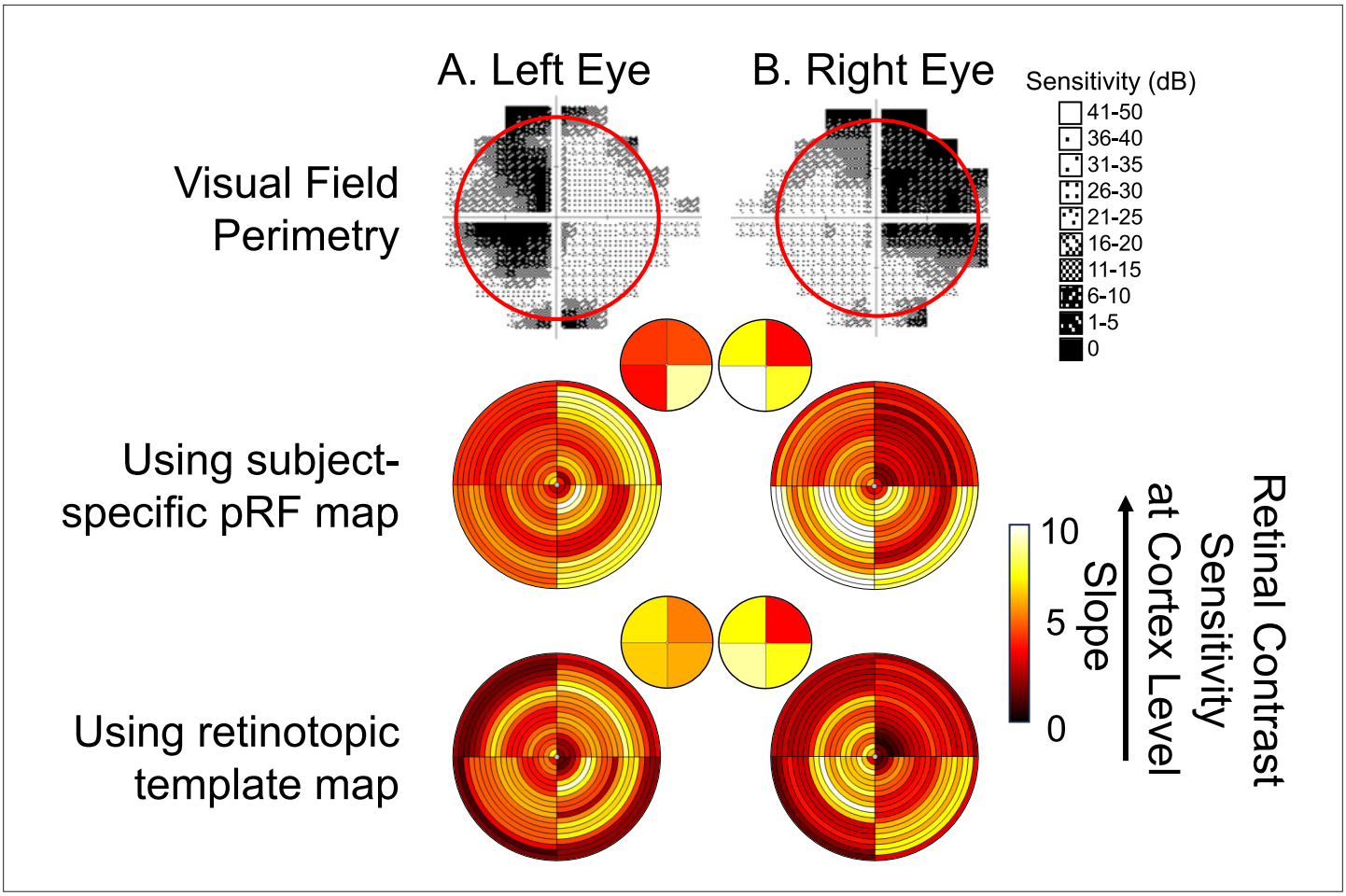


Figure 9. Correspondence between visual field perimetry map and V1 sensitivity map, in a patient with Leber Hereditary Optic Neuropathy. (**A**) Left eye. (**B**) Right eye. **Top row:** Gray scale visual field map obtained with the Compass fundus perimeter (CenterVue, Padova, Italy), using Standard Perimetry display convention. Sensitivity is represented with symbols and related dB intervals, with larger values describing better sensitivity. Red circle indicates the area of the visual space stimulated in the fMRI contrast sensitivity task. **Middle row:** Heatmap of V1 sensitivity (i.e., slopes) across the visual field. Here, we divided the space between the upper-left, upper-right, lower-left, and lower-right quadrants (as opposed to the left, right, upper, and lower quadrants used in previous sections), to match the layout of visual field perimetry maps. We also only show the responses to low spatial frequency condition (0.3 cpd) for visualization. Slope values were averaged for each visual quadrant and 1° eccentricity bin and projected back into the visual space, using the subject-specific pRF map. Color scale corresponds to the steepness of the slope estimate. For better visualization of sensitivity differences across quadrants, we also averaged the slopes between 0.5° and 20° eccentricities in each quadrant, generating a single slope value for each visual quadrant (inset heat plots). The range of slope values was reduced on the color scale for these inset plots. **Bottom row:** Heatmap of V1 sensitivity (i.e., slopes) across the visual field in response to the 0.3 cpd condition, using the Benson retinotopic template map instead of the pRF data.

key findings demonstrate that this approach can accurately quantify known variations in V1 contrast sensitivity across eccentricity and polar angle, recover simulated and pathological visual field losses, and produce consistent and reliable measures both at the group and individual participant levels. Crucially, the ability to visualize these sensitivity gradients was made possible by the large peripheral coverage provided by our large-field stimulation setup. Such coverage is particularly important for clinical applications, as it enables the detection of visual field losses beyond the macula (i.e., beyond 10° eccentricity) and the evaluation of residual peripheral vision in patients with macular-restricted damage. In doing so, this work provides a useful tool for advancing both basic visual neuroscience and translational research in clinical populations.

Validation of sensitivity variations across the visual field

Our method successfully captured the expected variations in cortical contrast sensitivity across the visual field. Consistent with previous behavioral and fMRI studies (***Aghajari et al., 2020***; ***Broderick***

et al., 2022; *D'Souza et al., 2016*; *Henriksson et al., 2008*; *Rovamo et al., 1984*; *Rovamo and Virsu, 1979*; *Welbourne et al., 2018*), we observed that V1 neuronal populations encoding the central visual field exhibited higher contrast sensitivity for high spatial frequency (SF) stimuli, while those encoding peripheral regions were more sensitive to low SF stimuli. This aligns with the understanding that SF tuning varies across the visual field due to smaller pRF sizes and larger cortical areas dedicated to central vision (*Himmelberg et al., 2023*).

Additionally, our study identified anisotropies in contrast sensitivity across visual field quadrants, mirroring findings from previous behavioral studies (*Barbot et al., 2021*; *Carrasco et al., 2022*; *Himmelberg et al., 2020*). Specifically, we found enhanced cortical sensitivity in V1 neuronal populations responding to horizontal versus vertical locations and to lower versus upper visual field locations. Unlike earlier fMRI studies (*Liu et al., 2006*; *O'Connell et al., 2016*), which either could not assess horizontal–vertical effects or used smaller region selections, our use of large-field stimuli enabled the detection of both upper-lower and horizontal–vertical asymmetries. Moreover, by modeling cortical contrast sensitivity across multiple contrast levels, we were able to identify subtle variations in V1 neuron sensitivity that single-threshold approaches might overlook.

We also observed intriguing variability in cortical visual field maps across healthy controls, and this variability was consistent across measures. This may reflect genuine individual differences in visual sensitivity that are relevant for behavioral performance. Alternatively, it could arise from factors such as local signal-to-noise differences driven by anatomical variability. However, the fact that maps derived from different spatial stimulus conditions showed markedly different patterns argues against a purely anatomical explanation and suggests that at least part of the variability is functional. Despite this inter-subject variability, variations in cortical contrast sensitivity across eccentricities and visual field quadrants were significant at the individual level indicating high sensitivity.

Reliability and sensitivity across sessions and robustness to eye movements

We also showed that our approach was reliable over time. We found consistent activation patterns and moderate-to-high correlations in slope estimates for the 0.3 cpd condition across two sessions, significantly higher than correlations across different stimuli conditions (i.e., 0.3 versus 3 cpd). High sensitivity and reliability are essential for detecting longitudinal changes in clinical groups, such as those occurring before and after sight-rescuing interventions. Fitting a contrast response function to the BOLD signal might offer robust estimates of visual function by minimizing the impacts of overall BOLD amplitude variability and arbitrary thresholds.

Crucially, one advantage of cortical visual field mapping is that the maps are inherently centered on the foveal confluence, providing a stable reference point for comparing responses across eccentricities. When combined with large-field, spatially homogeneous stimuli, this anchoring means that our approach should remain robust to moderate fixation variability and still quantify sensitivity changes across the visual field – provided that fixation instability does not exceed the stimulus extent (40° diameter).

When measuring the impact of eye movements, we found that spatial sensitivity patterns were largely preserved, even for extreme eye movements (emulating severe nystagmus). However, under the most extreme conditions, sensitivity estimates (i.e., slope values) were reduced, especially for high SF stimuli. This likely reflects image blurring from large rapid eye movements, which degrades high SF inputs and shifts activation toward neurons tuned to lower SFs. This aligns with evidence that nystagmus and large saccades impair perception of fine detail and grating stimuli due to retinal image slip (*Abadi and Bjerre, 2002*; *Dickinson and Abadi, 1985*; *Hertle et al., 2017*; *Randall et al., 2020*). While classic findings report suppression of low SF signals during saccades (*Burr et al., 1994*; *Ross et al., 2001*), our results suggest that high SF sensitivity may be more vulnerable to large eye movements when participants are presented with 2 Hz phase-flickering gratings. Further validation in clinical groups with naturally occurring fixation instability would further strengthen these conclusions.

Mapping simulated and pathology-driven vision loss

Our method successfully identified both simulated retinal loss in a healthy volunteer and real visual field loss in a patient with LHON. The signal drop observed in response to masking portions of the visual field in the healthy control was both large and significant at the individual level, as demonstrated

by non-overlapping 95% confidence intervals (***Figures 7B, C and 8B***). This provides proof-of-concept evidence that our approach can detect signal changes in individual patients, which is a critical requirement for clinical translation.

Unlike previous fMRI studies that used high-contrast stimuli (***Farahbakhsh et al., 2022***; ***Pawloff et al., 2023***; ***Ritter et al., 2019***), which may not accurately represent partial vision loss due to potential saturation effects and the stimulation of less sensitive retinal cells, our use of multiple contrast levels offers a more nuanced assessment of cortical contrast sensitivity. Combined with the large-field setup allowing stimulation up to 20° eccentricity, this approach may be particularly well-suited for evaluating treatment efficacy in cases of widespread and variable vision loss.

Future work will focus on further validating reconstruction accuracy under controlled conditions, including simulated scotomas of varying severity and location, expanding testing to larger patient cohorts, and establishing a normative dataset to contextualize patient data.

Limitations of pRF mapping, advances in structure-based templates, and future directions in brain-based visual field mapping

One limitation of this brain-based approach to visual field testing is its reliance on pRF mapping, which requires precise fixation and can be challenging to acquire in visually impaired patients. To mitigate this, we investigated the use of retinotopic templates based on anatomical landmarks (***Benson et al., 2014***; ***Benson and Winawer, 2018***), thereby reducing the need for pRF data collection and facilitating the mapping of brain responses to visual field positions. Particularly at large eccentricities, however, we initially observed inaccuracies between the template and individual retinotopy eccentricity estimates which led to substantial distortions in cortical visual field maps due to cortical magnification (see ***Appendix 1—figure 4***). To address this, we adjusted the Benson eccentricity estimates to align with the cortical magnification scaling function (***Horton and Hoyt, 1991***).

With this structure-based atlas, we successfully replicated key variations in visual field function (across eccentricity and polar quadrants), although sensitivity to more subtle differences (e.g., upper versus lower quadrant anisotropy) was reduced. This reduction may partly stem from differences in ROI definitions: a manually delineated V1 mask was used for the pRF-based data, while the Benson atlas mask was used for the adjusted Benson atlas analysis. Such differences could introduce minor error beyond the atlas/pRF mapping itself due to differences in the vertices included by each mask.

Beyond ROI considerations, we still observed differences in cortical sensitivity between pRF mapping and the adjusted Benson atlas – particularly in the periphery. Several factors likely contribute to this. First, individual differences in the relationship between cortical structure and retinotopy are not fully captured by the template. Second, the Benson atlas has never been fit with empirical data more eccentric than approximately 20°, which naturally limits its precision in the far periphery. Third, because of cortical magnification, any small inaccuracy at larger eccentricities has a disproportionately large effect, making peripheral vertices more susceptible to mis-assignment than central ones. These influences introduce systematic distortions in cortical visual field maps rather than random noise and thus remain consistent across timepoints – an important point when assessing longitudinal changes (e.g., aging or gene-therapy interventions). Importantly, the spatial gradients in cortical contrast sensitivity were preserved across both the pRF and Benson atlas approaches, indicating that minor ROI differences do not affect our conclusions. Together, these findings show that the Benson atlas remains a useful alternative when pRF mapping is not feasible.

It is also promising that cortical structure-based templates can successfully recover visual field loss through simulation or the neurodegenerative disease LHON. Critically, in patient groups with severe impairment such as LHON, where it is often very challenging or impossible to obtain reliable measures, even imperfect mapping between the brain and visual field could offer important improvements over available solutions for tracking functional change, and where they stem from. Further enhancing the alignment between retinotopic template atlases and individual retinotopic tuning could improve this approach further, for example, by integrating them with functional measures using Bayesian methods (***Benson and Winawer, 2018***). In parallel, geometric deep learning frameworks such as DeepRetinotopy (***Ribeiro et al., 2021***) could also offer anatomy-driven predictions from structural MRI, and combining these strategies may yield more accurate and generalizable retinotopic reconstructions.

While our method demonstrated high accuracy and reliability in sighted controls, further validation in patients is necessary to ensure the generalizability of our approach to measuring pathology. Next

steps in this work will therefore involve testing larger patient cohorts with diverse forms of vision loss, validating the approach for tracking pathology over time, and investigating how cortex-based visual field measures relate to and complement other visual field and retinal integrity indices including Compass measures and OCT-derived retinal layer thickness. For example, while we reasoned that using a single high-contrast stimulus is likely to give less reliable measures for various reasons outlined above, this needs to be tested empirically. It also remains unclear whether the square root contrast response function is optimal for patients, who are likely to show different non-linearities in their contrast response. In addition, comparing the cortical contrast sensitivity modeling approach presented here with alternative frameworks (e.g., neural contrast sensitivity functions proposed by ***Roelofzen et al., 2025***) will be another interesting direction for future research. Finally, more extensive mapping of the SF and contrast sensitivity spaces could offer additional informative measures such as cortical acuity and SF preferences, provided such measures are feasible with patient-friendly protocols.

Conclusion

In sum, brain-based contrast sensitivity measures could significantly enhance the accurate characterization of visual field function in blinding diseases, by addressing limitations of traditional visual field tests that are subjective, time-consuming, and challenging for patients with severe sight loss. By providing a reliable, quantitative measure of cortical contrast sensitivity across the visual field, fMRI may help facilitate the monitoring of disease progression and recovery, including interventions like gene therapy. Combined with our large-field stimulation setup and fixation-free approaches to linking cortical sensitivity estimates to visual field locations, this method is well-suited for a wide range of visual impairments, addressing a pressing challenge in the evaluation of current clinical trials. Additionally, linking brain-based variations in function across the visual field to behavioral performance (e.g., perimetry, microperimetry) and retinal structure (fundus imaging, retinal thickness from Optical Coherence Tomography), could help bridge the gap between neural measures and functional outcomes. Such integration would provide deeper insights into developmental, learning, and vision loss mechanisms.

In conclusion, integrating cortical contrast sensitivity testing with large-field stimulation and a calibrated retinotopic atlas provides a promising tool for characterizing visual field impairments, and could offer a valuable addition to existing measures of visual field loss.

Methods

Participants

We collected data from 7 healthy controls (mean ± SD: 29.6 ± 4.7 yo; 1 M). All controls either had normal or corrected to normal vision, with no other ocular pathologies, and were recruited from the local staff and student pool at the University College of London. Each control completed both the population receptive field (pRF) mapping and the fMRI contrast sensitivity task. To assess measurement repeatability, four participants (C2, C4, C5, and C6) performed the contrast sensitivity task twice. Additionally, one participant (C5) repeated the task under two simulated vision loss conditions (ring or quadrant loss), and two others (C5 and C6) completed it with different levels of eye movement.

We also recruited a patient with LHON (M, 45.5 years old, mutation: m.11778G>A, disease duration: 36.1 years), who presented with relatively stable fixation and was able to complete both the pRF mapping and the fMRI contrast sensitivity task. All participants signed a written informed consent to participate in the study, and this study was approved by HRA/HCRW and Research Ethics Committee (IRAS 258959; REC 20/YH/0336).

Stimulus and apparatus

Stimuli were programmed in MATLAB 2020b (MathWorks, Natick, Massachusetts, USA) using the Psychtoolbox-3, and displayed using an EPSON LB-1100U projector (resolution: 1920x1200 pixels, 60 Hz, projected area: 43.2 × 27 cm). Because the projector was too bright and to reduce discomfort in the scanner, a circular neutral density filter (ND4 Plus+; Urth, Byron Bay, Australia) was placed in front of the projector to reduce light intensity by four times without altering the colors. The projector was also gamma-corrected to ensure accurate representation of the intended contrast levels and spatial frequencies used in our experiments. In all tasks, stimuli were embedded in a circular aperture

of 42.3° × 42.3° diameter. To achieve the large field-of-view, the front part of the 64-channel MRI coil was removed, and stimuli were back-projected onto a screen positioned close to the participant's head inside the bore (see ***Appendix 1—figure 1***). Participants viewed the stimuli through a mirror, for a total viewing distance of 34 cm. Throughout the session, participants were constantly reminded to remain still to minimize head and body motion, and eye motion and alertness were monitored using an EyeLink 1000Plus device (SR Research, Ottawa, Canada). In all tasks, participants were asked to report when the color of a central fixation dot changed.

fMRI contrast sensitivity task

Participants were presented binocularly with achromatic sine-wave gratings, flickering at a temporal frequency of 2 Hz and varying in contrast levels and spatial frequencies. Contrast levels were defined as Michelson contrast ($C = \frac{L_{max} - L_{min}}{L_{max} + L_{min}}$), where Lmax and Lmin are maximum and minimum luminance. Each stimulus, presented for 13 s, featured a specific contrast level (either 7.5, 42.2, 60, or 100%) and SF (either 0.3 or 3 ccpd). Stimuli were then followed by 2 s of a gray background (0% contrast) to minimize the experience of after-effects. Each combination of contrast level and SF was shown three times within a run, arranged in a pseudo-random sequence, for a total of 9 repetitions per combination (i.e., 3 runs). Eight additional blocks of 15-s rest periods with a gray background were introduced to allow sufficient baseline. Four participants (C2, C4, C5, and C6) were invited for a second session in which they repeated the task to assess the reliability of the measures.

For six control participants (C1–C6), gratings were initially presented with a fixed horizontal orientation. In an updated version of the task – used for C7, cases of simulated eye movement, cases of artificial scotoma, and the LHON patient – the orientation varied every 5 s among four angles (−45°, 0°, 45°, and 90°). Contrast sensitivity patterns were consistent across single- and multiple-orientation conditions, including in participants who completed both versions, indicating robustness across orientation-tuned populations.

Effect of eye movement

Participants C5 and C6 also performed a version of the task designed to test the effect of eye movements. In this version, saccades were elicited by randomly and rapidly shifting the fixation dot away from central fixation (C5: 2° and 5° from fixation and random motion; C6: up to 2° from fixation). Participant C5 was tested using 0.3 and 3 cpd gratings at four contrast levels (7.5, 42.2, 60, and 100%), while participant C6 was tested only under the low SF condition (0.3 cpd).

Fixation stability was assessed for each fMRI run using the BCEA, which estimates the area (in degrees² or arcmin²) of an ellipse that contains approximately 95% of fixation points. BCEA was calculated using the formula: $BCEA = 2 * k * \pi * \sigma_h * \sigma_v * \sqrt{1 - \rho^2}$, as described by ***Morales et al., 2016***. In this expression, σ_h and σ_v represent the standard deviations of eye position in the horizontal and vertical directions, respectively, while ρ corresponds to the Pearson correlation coefficient between horizontal and vertical eye positions. The constant k determines the size of the ellipse based on the desired probability area, defined by the relationship $P = 1 - e^{-k}$, with P set to 0.95 in this study. A smaller BCEA indicates greater fixation stability.

Simulated vision loss

One healthy control participant (C5) also performed a version of the task designed to simulate two forms of visual input loss (i.e., artificial scotoma). These simulations were implemented by: (1) masking a region of the visual field with a gray, annular ring, covering 3°–8° eccentricity, and (2) masking the upper-right visual quadrant using a gray quarter-sector overlay. The stimuli and contrast levels used in this task were identical to those described in the original task.

pRF mapping

To investigate how distinct regions of the visual field map onto the cortex, we collected pRF mapping data using a standard ring-and-wedge stimulus (***Dumoulin and Wandell, 2008***). Participants were presented binocularly with a black-and-white checkerboard, phase-flickering at a temporal frequency of 2 Hz, and at maximum contrast level. The stimulus spanned up to the boundaries of the circular aperture (i.e., 42.3° × 42.3° diameter) and was scaled across eccentricity to account for cortical magnification. This scaling was implemented by applying a logarithmic transformation of retinal radius,

such that radial checker boundaries were defined in log-eccentricity space ($\log(r)$, where r denotes to eccentricity relative to the fixation target). This produced an exponential increase in checker size with eccentricity (scaling factor = 3.2; ~1.37 times increase per radial step), resulting in lower spatial-frequency content at larger eccentricities – consistent with known variations in V1 spatial-frequency tuning. Because this eccentricity-dependent scaling assumes precise fixation, it can be challenging for individuals with central vision loss, further motivating the use of Benson atlas templates in such populations. Three runs of 352 volumes were collected per participant.

MRI acquisition

Data were collected at the Birkbeck-UCL Centre for NeuroImaging (BUCNI, London, UK), on a Siemens PRISMA 3 Tesla scanner.

Functional data were acquired using a 64-channel head coil with the front part removed, to allow an unobstructed view of the screen while ensuring enough signal from the remaining 40 effective channels covering the side and back of the head. T2*-weighted echo-planar imaging were collected with an accelerated multiband sequence kindly provided by CMRR (version R016a, https://www.cmrr.umn.edu/multiband; ***Cauley et al., 2014***; ***Xu et al., 2013***); multi-band factor: 4, voxel resolution: 2 mm isotropic, FOV: 212 × 212 × 96 mm, flip angle: 60°, repetition time (TR): 1000 ms, echo time (TE): 35.2 ms, echo spacing: 0.56 ms, bandwidth: 2620 Hz/Px, with 48 transverse slices angled to be approximately parallel to the calcarine sulcus while avoiding the orbital cavities. The same sequence was used to acquire four additional scans in the opposite phase-encoding direction, to allow B0 deformation correction in the pre-processing steps.

A T1-weighted structural image was acquired with a 32-channel coil, using MPRAGE sequence (voxel resolution: 1 mm isotropic, 208 slices, FOV: 256 × 256 × 208 mm, flip angle: 7°, TR = 2300 ms, TE = 2.98 ms, TI = 900 ms, bandwidth: 240 Hz/Px, echo spacing: 7.1 ms, acquisition time: 5 min 30 s).

Data analysis

Segmentation of the anatomical scan and reconstruction of cortical surfaces were performed in FreeSurfer 7.1.1.

Functional data were pre-processed using a combination of AFNI 24.1.22, FreeSurfer and FSL 6.0.7.12 commands. The following steps were followed for both the contrast sensitivity task and the pRF mapping task. First, initial correction for distortions caused by field inhomogeneity was performed using a blip-up/blip-down approach (AFNI's unWarpEPI.py program), and the first 4 volumes of each run were discarded using FSL's fslroi program. Then an alignment scan was created from the volume out of all collected runs that contained the least amount of voxel outliers using AFNI's 3dToutcount, 3dTstat and 3dcalc programs. This alignment scan was then co-registered to the MPRAGE image using FreeSurfer's bbregister program, resulting in a rigid-body transformation matrix. In case of misregistration, the alignment scan was defined as one of the single-band reference scans, before re-running the co-registration step. Motion correction was then carried out by aligning each functional volume from all runs to the previously defined alignment scan using AFNI's 3dvolreg program.

Processing of the contrast sensitivity task

To accurately capture neural activity across various eccentricities and polar angle locations, minimal smoothing (0.5 mm FWHM Gaussian blur) was applied to the contrast sensitivity task data using FSL's 3dmerge program. This was done to meet the minimum requirements of the general linear model (GLM) module in SPM. The contribution of each contrast/SF combination to the BOLD signal was modeled using the GLM approach in SPM12 (https://www.fil.ion.ucl.ac.uk/spm/), with motion parameters as additional regressors. This step resulted in volumetric images of β-values, each reflecting the specific contribution of a given contrast/SF combination to the baseline BOLD signal. These resulting β-images were then projected onto the individual's cortical surface using FreeSurfer's mri_vol2surf program, with no surface smoothing and the default fractional projection along surface of 0.5. The latter sets the fraction (0,1) of the cortical thickness at each vertex to project along the surface. Surface-projected β-images were finally converted into a MATLAB-compatible format for further analysis using SamSrf's samsrf_mgh2srf program.

Processing of pRF mapping task

Pre-processed volumes from the pRF mapping task were projected onto the cortical surface using FreeSurfer's mri_vol2surf program. Here, we used the previously generated rigid-body transformation matrix to ensure accurate spatial alignment and smoothed on the cortical surface with a Gaussian kernel with an FWHM of 3 mm.

During pRF model fitting, pRF centers were allowed to extend beyond the stimulated visual field to improve model stability near stimulus boundaries – up to approximately 1.5 times the maximum stimulus eccentricity (~30°). Eccentricity was sampled on a logarithmically spaced grid defined as 2^x, with x ranging from −5 to 0.6 in steps of 0.2, and then scaled by the maximum stimulus eccentricity (20°) to express pRF centers in degrees of visual angle. This sampling scheme provided finer resolution near the fovea and progressively coarser sampling at larger eccentricities, consistent with cortical magnification principles.

The resulting outputs were then converted into a MATLAB-compatible format for further analysis. pRF estimates were computed by fitting a 2D Gaussian model to the data, using the SamSrf toolbox (version 7.13; https://github.com/samsrf; ***SamSrf, 2026***), resulting in three pRF parameters for each vertex on the cortical surface: the *x*- and *y*-coordinates of the pRF center, and the pRF size (σ). Eccentricity and polar angle maps were computed from the *x*- and *y*-coordinates.

Regions-of-interest

In this study, we were interested in how visual information across the visual field is processed in early visual areas, notably in the primary visual cortex V1. Early visual regions were manually delineated for each participant in SamSrf v7.13, based on the output of the pRF fitting procedure and standard functional criteria to identify borders between V1, V2, and V3 (***DeYoe et al., 1996***; ***Engel et al., 1997***; ***Sereno et al., 1995***). In this report, we focused our interest on V1, given its crucial role in the initial processing of basic visual features like SF and contrast. For all subsequent analyses of cortical contrast sensitivity, pRF centers outside the stimulated 20° eccentricity were excluded. Similarly, although the Benson atlas provides eccentricity estimates extending far beyond the stimulated range (up to ~90°), only values within 20° were retained to maintain consistency across pRF-based and atlas-based analyses.

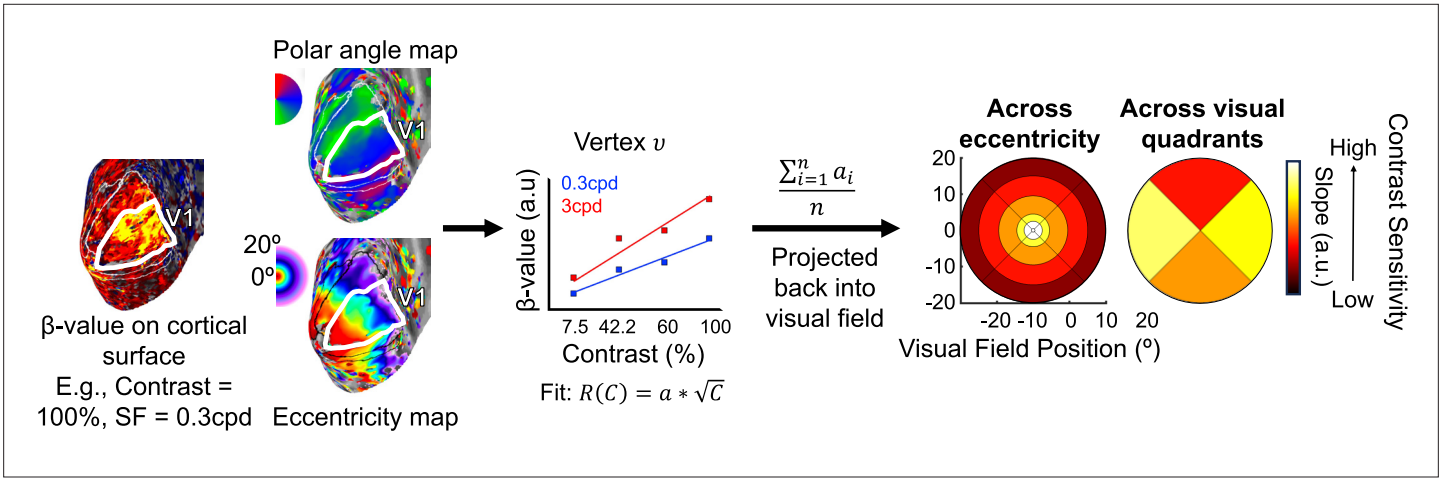


Figure 10. Estimation of cortical contrast sensitivity across the visual field. Participants performed two fMRI tasks in the scanner: a contrast sensitivity task and a pRF mapping task. For each individual and tested spatial frequency, the contribution of each stimulus contrast level to the BOLD signal in the contrast sensitivity task was estimated using a general linear model (GLM) approach. Resulting β-coefficients for each contrast level were then projected onto the individual's cortical surface. For each vertex in V1, a square root function ($R(C) = a * \sqrt{C}$) was then fitted to these data, taking the estimated slope *a* as a measure of cortical contrast sensitivity. V1 slopes were finally averaged across vertices based on their eccentricity and polar angle preference as estimated with pRF mapping, and across participants. Mean slopes were then projected back into the visual space, producing a heatmap projection of V1 contrast sensitivity across eccentricities and along visual field quadrants.

Quantifying eccentricity- and location-dependent variations in sensitivity

Using subject-specific pRF estimates

At this stage, for each vertex on the cortical surface, we obtained β-values for each tested contrast/SF combination in the contrast sensitivity task, as well as pRF parameters resulting from the fitting of the pRF model to the pRF data (***Figure 10***). β-values from the contrast sensitivity task in each vertex were then filtered based on ROI location (V1) and pRF parameters ($R^2 \geq 0.05$; pRF size: $\sigma \leq 6$).

To assess contrast sensitivity, we modeled the neural response (i.e., β-values) in V1 as a linear function of the square root of the contrast values ($R\left(C\right) = a * \sqrt{C}$). This model rests on the assumption of a monotonic relationship between the presented stimulus contrast level and the resulting BOLD response and has been used in previous work by Buracas and colleagues to investigate contrast sensitivity at the cortex level in healthy controls (***Buracas et al., 2005***; ***Buracas and Boynton, 2007***). Steeper slopes within this context indicate greater V1 contrast sensitivity.

We fit this model for each vertex separately, for each participant and SF (0.3 and 3 cpd) condition. The intercept was constrained to be zero, as the distribution of β-values is expected to be centered on zero when the contrast is zero (i.e., when no stimulus is presented). Next, the resulting V1 slope estimates were binned and averaged over five regions using pRF eccentricity estimates: 0.5°–2.5°, 2.5°–4.5°, 4.5°–9.5°, 9.5°–15°, and 15°–20°. These bins relate to the clinical definition of visual space based on anatomical landmarks, corresponding to the fovea, parafovea, perifovea, and two near-periphery regions, respectively. Similarly, slope estimates were spatially constrained within a±45°-wedge centered on each cardinal meridian to investigate asymmetries as a function of pRF polar angle locations, thus dividing the visual space between the upper, lower, left, and right quadrants. These wedges were also derived from the polar angle estimates obtained with pRF mapping.

For each participant, average slopes for each eccentricity bin and polar angle wedge were then projected back into their corresponding visual field locations. This resulted in heat-maps of V1 contrast sensitivity across eccentricities and visual field quadrants, for each tested SF condition at an individual level (***Figure 10***). Finally, average slopes for each eccentricity and polar angle bin from each participant were used to compute the group-level average.

Using calibrated Benson retinotopic template atlas

The same approach was used to quantify changes in V1 contrast sensitivity across the visual field, using a retinotopic template (***Benson et al., 2014***; ***Benson and Winawer, 2018***) instead of pRF mapping. This template was fitted to each subject's anatomical MPRAGE image using the Python library neuropythy (***Benson and Winawer, 2018***), which provided automatic delineation of early visual regions, based on FreeSurfer's anatomical alignment. Additionally, it offered eccentricity and polar angle estimates for each vertex on the cortical surface. The advantage of this method over pRF mapping is that it does not require fixation or pRF scanning, making it a valuable tool to use when scan time is valuable or in populations where good fixation is hard to achieve.

We initially observed inaccuracies between the template and individual retinotopy eccentricity estimates which led to substantial distortions in cortical visual field maps due to cortical magnification – especially in peripheral locations (see ***Appendix 1—figure 4***). To enhance the accuracy of eccentricity estimates in the template map, we aligned the distribution of eccentricity values from the fitted Benson template atlas with Horton and Hoyt's model (***Horton and Hoyt, 1991***; ***Figure 11A***). This model suggests that the linear cortical magnification factor (M_{linear} in mm/°) is inversely proportional to eccentricity (E in degrees), expressed as $M_{linear} = \frac{scale}{E+shape}$, with the normalizing parameter $shape$ equal to 0.75°, as measured by ***Horton and Hoyt, 1991***. Using this relationship, we first estimated for each hemisphere the *scale* value based on each individual's V1 surface area (from the Benson V1 label) and the minimum and maximum eccentricities considered in the model (0° and 90°). The mean *scale* value for the left and right V1 hemispheres across all tested controls were 15.0 ± 0.99 and 16.0 ± 1.09, respectively. In comparison, ***Horton and Hoyt, 1991*** measured a mean *scale* of 17.3 mm. The mean V1 surface areas for the left and right hemispheres were 2700.7 ± 358.7 and 3067.7 ± 416.3 mm^2.

We then defined a function $f\left(r\right)$ that describes how the surface area of V1 changes with eccentricity (***Equation 1***; ***Figure 11A***). This was achieved by integrating Horton and Hoyt's function over the visual field, resulting in an equation that calculates the amount of V1 surface area from the foveal confluence up to a particular eccentricity (r). Next, we sorted the input eccentricity values and calculated the

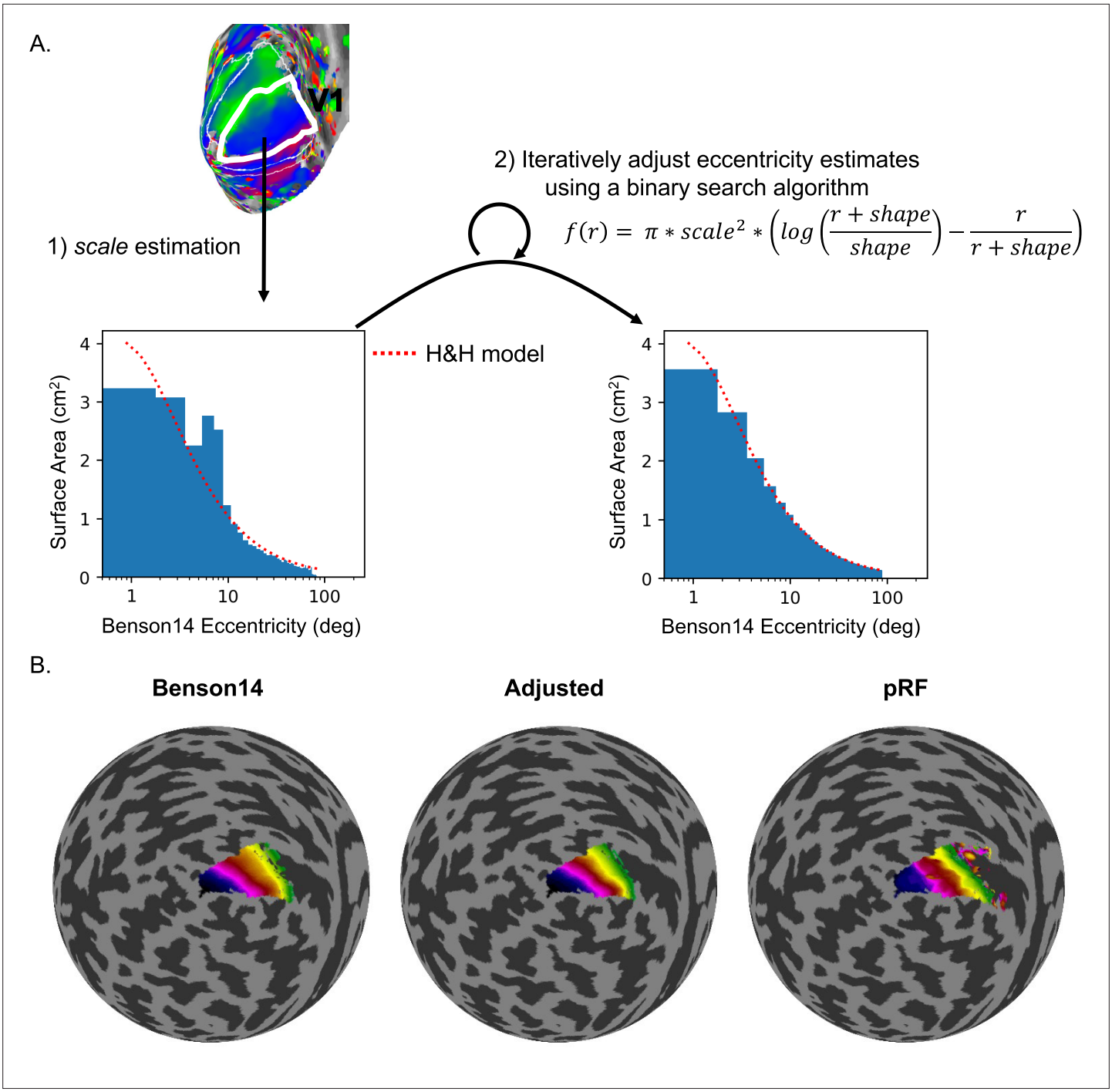


Figure 11. Eccentricity alignment and surface area estimation in V1. (**A**) For each hemisphere, the scale parameter in Horton and Hoyt's linear magnification model $M_{\text{linear}} = \frac{\text{scale}}{E+0.75}$ was estimated from individual V1 surface area and the 0°–90° eccentricity range. Using this, we derived a cumulative surface-area function $f(r)$, which gives the total cortical area of V1 representing eccentricities from 0° to r. For visualization, the histograms show the differential form of this function – that is, the surface-area density as a function of eccentricity. This corresponds to the derivative $\frac{df}{dr}$, which reflects the areal magnification (denoted $m^*(r)$) integrated over polar angle. This representation provides a clearer view of how cortical surface area is distributed across eccentricities while remaining consistent with the underlying cumulative function $f(r)$. Adjusted eccentricity values were obtained by iteratively matching the empirical surface-area distribution to the model using a binary search procedure. (**B**) Comparison of eccentricity maps generated using the Benson template, the adjusted eccentricity values, and population receptive field (pRF) estimates, showing improved alignment with empirical data.

cumulative surface areas. A numerical method was then employed to find the eccentricity values that match the desired distribution. This method involved iteratively adjusting the range of possible values until the calculated values closely matched the desired values. Finally, the adjusted eccentricity values were returned in their original order and values from both hemispheres were merged to provide bilateral eccentricity estimates.

$$f(r) = \pi * scale^2 * \left(\log\left(\frac{r + shape}{shape}\right) - \frac{r}{r + shape}\right). \quad (1)$$

Acknowledgements

This work was funded by Moorfields Eye Charity PhD Studentship GR001315 (London, UK), the Wellcome Career Development Award (306332/Z/23/Z; London, UK), and the Birkbeck-UCL Centre for NeuroImaging (BUCNI; London, UK). The funders had no role in study design, data collection, and analysis, decision to publish, or preparation of the manuscript. PYWM is supported by an Advanced Fellowship Award (NIHR301696) from the UK National Institute of Health Research (NIHR). PYWM also receives funding from Fight for Sight (UK), the Isaac Newton Trust (UK), Moorfields Eye Charity (GR001376), the Addenbrooke's Charitable Trust, the National Eye Research Centre (UK), the International Foundation for Optic Nerve Disease (IFOND), the NIHR as part of the Rare Diseases Translational Research Collaboration, the NIHR Cambridge Biomedical Research Centre (NIHR203312), and the NIHR Biomedical Research Centre based at Moorfields Eye Hospital NHS Foundation Trust and UCL Institute of Ophthalmology (NIHR203322). The views expressed are those of the author(s) and not necessarily those of the NHS, the NIHR or the Department of Health. We extend our thanks to Simon Richardson and Oliver Josephs for their assistance in the design and conception of the large-field setup.

Additional information

Competing interests

Tessa M Dekker: Reviewing editor, eLife. The other authors declare that no competing interests exist.

Funding

Funder	Grant reference number	Author
Moorfields Eye Charity	PhD Studentship GR001315	Tessa M Dekker
Wellcome Trust	10.35802/306332	Tessa M Dekker
Birkbeck-UCL Centre for NeuroImaging, London, UK		Hugo T Chow-Wing-Bom Tessa M Dekker

The funders had no role in study design, data collection, and interpretation, or the decision to submit the work for publication. For the purpose of Open Access, the authors have applied a CC BY public copyright license to any Author Accepted Manuscript version arising from this submission.

Author contributions

Hugo T Chow-Wing-Bom, Conceptualization, Data curation, Software, Formal analysis, Funding acquisition, Validation, Investigation, Visualization, Methodology, Writing – original draft, Project administration, Writing – review and editing; Matteo Lisi, Software, Formal analysis, Methodology, Writing – original draft; Noah C Benson, Software, Formal analysis, Methodology, Writing – original draft, Writing – review and editing; Freya Lygo-Frett, Supervision, Methodology, Writing – original draft; Patrick Yu-Wai-Man, Resources, Supervision, Writing – original draft; Frederic Dick, Resources, Supervision, Funding acquisition, Writing – original draft; Roni O Maimon-Mor, Conceptualization, Investigation, Writing – original draft; Tessa M Dekker, Conceptualization, Resources, Supervision,

Funding acquisition, Validation, Visualization, Methodology, Writing – original draft, Writing – review and editing

Author ORCIDs
Hugo T Chow-Wing-Bom https://orcid.org/0000-0003-3348-3005
Noah C Benson https://orcid.org/0000-0002-2365-8265
Frederic Dick https://orcid.org/0000-0002-2933-3912
Roni O Maimon-Mor https://orcid.org/0000-0001-5262-9976
Tessa M Dekker https://orcid.org/0000-0002-3616-2859

Ethics
All participants provided written informed consent prior to taking part in the research, including consent for their anonymized data to be published. Experimental procedures involving human participants were conducted in accordance with the Declaration of Helsinki and approved by the HRA/HCRW and Research Ethics Committee (IRAS 258959; REC 20/YH/0336).

Peer review material
Version of Record:
Reviewer #1 (Public review): https://doi.org/10.7554/eLife.105930.3.sa1
Reviewer #2 (Public review): https://doi.org/10.7554/eLife.105930.3.sa2
Reviewer #3 (Public review): https://doi.org/10.7554/eLife.105930.3.sa3
Author response https://doi.org/10.7554/eLife.105930.3.sa4

Reviewed preprint v2
Reviewer #1 (Public review): https://doi.org/10.7554/eLife.105930.2.sa3
Reviewer #2 (Public review): https://doi.org/10.7554/eLife.105930.2.sa2
Reviewer #3 (Public review): https://doi.org/10.7554/eLife.105930.2.sa1
Author response: https://doi.org/10.7554/eLife.105930.2.sa0
eLife Assessment https://doi.org/10.7554/eLife.105930.2.sa4

Reviewed preprint v1
Reviewer #1 (Public review): https://doi.org/10.7554/eLife.105930.1.sa2
Reviewer #2 (Public review): https://doi.org/10.7554/eLife.105930.1.sa1
Reviewer #3 (Public review): https://doi.org/10.7554/eLife.105930.1.sa0
eLife Assessment https://doi.org/10.7554/eLife.105930.1.sa3

Additional files

Supplementary files
MDAR checklist

Data availability
All post-processed and anonymized data are available on Zenodo (https://doi.org/10.5281/zenodo.19051439). Codes to reproduce the figures from the provided dataset are available on GitHub (https://github.com/HugoCWB/ChowWingBomEtAl_2025_eLife, copy archived at ***Chow-Wing-Bom, 2026b***). Codes to adjust the Benson maps' eccentricity are available on GitHub (https://github.com/HugoCWB/AdjustEccTool, copy archived at ***Chow-Wing-Bom and Benson, 2026a***). A Docker image for the Benson eccentricity adjustment toolbox is also available on Zenodo (https://doi.org/10.5281/zenodo.18770065). The original raw data cannot be shared publicly because of participant consent and ethical approval restrictions. Access can be requested by emailing the corresponding author, Dr Hugo Chow-Wing-Bom (hugo.chow-wing-bom.15@ucl.ac.uk), or the senior author, Prof Tessa Dekker (t.dekker@ucl.ac.uk). Requests should include a brief project proposal and will be assessed by Prof Dekker and the study team. Access will be granted subject to a data sharing agreement between the requesting organisation and UCL.

The following datasets were generated:

Author(s)	Year	Dataset title	Dataset URL	Database and Identifier
Chow-Wing-Bom H, Lisi M, Benson N, Lygo-Frett F, Yu-Wai-Man P, Dick F, Maison-Mor R, Dekker T	2026	Dataset for Chow-Wing-Bom et al., 2025, eLife	https://doi.org/10.5281/zenodo.19051439	Zenodo, 10.5281/zenodo.19051439
Chow-Wing-Bom H, Benson N	2026	Benson Map Eccentricity Adjustment Tool	https://doi.org/10.5281/zenodo.18770065	Zenodo, 10.5281/zenodo.18770065

References

Abadi RV, Bjerre A. 2002. Motor and sensory characteristics of infantile nystagmus. *The British Journal of Ophthalmology* **86**:1152–1160. DOI: https://doi.org/10.1136/bjo.86.10.1152, PMID: 12234898

Aghajari S, Vinke LN, Ling S. 2020. Population spatial frequency tuning in human early visual cortex. *Journal of Neurophysiology* **123**:773–785. DOI: https://doi.org/10.1152/jn.00291.2019, PMID: 31940228

Alvarez GA. 2011. Representing multiple objects as an ensemble enhances visual cognition. *Trends in Cognitive Sciences* **15**:122–131. DOI: https://doi.org/10.1016/j.tics.2011.01.003

Barbot A, Xue S, Carrasco M. 2021. Asymmetries in visual acuity around the visual field. *Journal of Vision* **21**:2. DOI: https://doi.org/10.1167/jov.21.1.2, PMID: 33393963

Bates D, Mächler M, Bolker B, Walker S. 2015. Fitting linear mixed-effects models using lme4. *Journal of Statistical Software* **67**:v067.i01. DOI: https://doi.org/10.18637/jss.v067.i01

Benson NC, Butt OH, Brainard DH, Aguirre GK. 2014. Correction of distortion in flattened representations of the cortical surface allows prediction of V1-V3 functional organization from anatomy. *PLOS Computational Biology* **10**:e1003538. DOI: https://doi.org/10.1371/journal.pcbi.1003538, PMID: 24676149

Benson NC, Winawer J. 2018. Bayesian analysis of retinotopic maps. *eLife* **7**:e40224. DOI: https://doi.org/10.7554/eLife.40224, PMID: 30520736

Bourne R, Steinmetz JD, Flaxman S, Briant PS, Taylor HR, Resnikoff S, Casson RJ, Abdoli A, Abu-Gharbieh E, Afshin A, Ahmadieh H, Akalu Y, Alamneh AA, Alemayehu W, Alfaar AS, Alipour V, Anbesu EW, Androudi S, Arabloo J, Arditi A, et al. 2021. Trends in prevalence of blindness and distance and near vision impairment over 30 years: an analysis for the Global Burden of Disease Study. *The Lancet Global Health* **9**:e130–e143. DOI: https://doi.org/10.1016/S2214-109X(20)30425-3

Broderick WF, Simoncelli EP, Winawer J. 2022. Mapping spatial frequency preferences across human primary visual cortex. *Journal of Vision* **22**:3. DOI: https://doi.org/10.1167/jov.22.4.3, PMID: 35266962

Buracas GT, Fine I, Boynton GM. 2005. The relationship between task performance and functional magnetic resonance imaging response. *The Journal of Neuroscience* **25**:3023–3031. DOI: https://doi.org/10.1523/JNEUROSCI.4476-04.2005, PMID: 15788758

Buracas GT, Boynton GM. 2007. The effect of spatial attention on contrast response functions in human visual cortex. *The Journal of Neuroscience* **27**:93–97. DOI: https://doi.org/10.1523/JNEUROSCI.3162-06.2007, PMID: 17202476

Burr DC, Morrone MC, Ross J. 1994. Selective suppression of the magnocellular visual pathway during saccadic eye movements. *Nature* **371**:511–513. DOI: https://doi.org/10.1038/371511a0, PMID: 7935763

Carrasco M, Roberts M, Myers C, Shukla L. 2022. Visual field asymmetries vary between children and adults. *Current Biology* **32**:R509–R510. DOI: https://doi.org/10.1016/j.cub.2022.04.052, PMID: 35671720

Cauley SF, Polimeni JR, Bhat H, Wald LL, Setsompop K. 2014. Interslice leakage artifact reduction technique for simultaneous multislice acquisitions. *Magnetic Resonance in Medicine* **72**:93–102. DOI: https://doi.org/10.1002/mrm.24898

Chow-Wing-Bom H, Benson N. 2026a. AdjustEccTool. swh:1:rev:85bba2af3530612050f0166f20343594395e3f30. Software Heritage. https://archive.softwareheritage.org/swh:1:dir:040551a10851989858bc085f62241cb838b26024;origin=https://github.com/HugoCWB/AdjustEccTool;visit=swh:1:snp:a1104936c5c1c1b0ac9711b6ad406e7273cd14a9;anchor=swh:1:rev:85bba2af3530612050f0166f20343594395e3f30

Chow-Wing-Bom H. 2026b. ChowWingBomEtAl_2025_eLife. swh:1:rev:0014b8fa0797ece45b1bf5cadca99a20e4999f25. Software Heritage. https://archive.softwareheritage.org/swh:1:dir:361ff03e0fb8b3d3a2bcf5c19d29421d3b1ab7c0;origin=https://github.com/HugoCWB/ChowWingBomEtAl_2025_eLife;visit=swh:1:snp:2d16bd12b8e96e065d46a3ff977a2beea5099ca3;anchor=swh:1:rev:0014b8fa0797ece45b1bf5cadca99a20e4999f25

DeYoe EA, Carman GJ, Bandettini P, Glickman S, Wieser J, Cox R, Miller D, Neitz J. 1996. Mapping striate and extrastriate visual areas in human cerebral cortex. *PNAS* **93**:2382–2386. DOI: https://doi.org/10.1073/pnas.93.6.2382

Dickinson CM, Abadi RV. 1985. The influence of nystagmoid oscillation on contrast sensitivity in normal observers. *Vision Research* **25**:1089–1096. DOI: https://doi.org/10.1016/0042-6989(85)90097-5, PMID: 4071987

D'Souza DV, Auer T, Frahm J, Strasburger H, Lee BB. 2016. Dependence of chromatic responses in V1 on visual field eccentricity and spatial frequency: an fMRI study. *Journal of the Optical Society of America A* **33**:A53. DOI: https://doi.org/10.1364/JOSAA.33.000A53

Dumoulin SO, Wandell BA. 2008. Population receptive field estimates in human visual cortex. *NeuroImage* **39**:647–660. DOI: https://doi.org/10.1016/j.neuroimage.2007.09.034

Engel SA, Glover GH, Wandell BA. 1997. Retinotopic organization in human visual cortex and the spatial precision of functional MRI. *Cerebral Cortex* **7**:181–192. DOI: https://doi.org/10.1093/cercor/7.2.181, PMID: 9087826

Farahbakhsh M, Anderson EJ, Maimon-Mor RO, Rider A, Greenwood JA, Hirji N, Zaman S, Jones PR, Schwarzkopf DS, Rees G, Michaelides M, Dekker TM. 2022. A demonstration of cone function plasticity after gene therapy in achromatopsia. *Brain* **145**:3803–3815. DOI: https://doi.org/10.1093/brain/awac226, PMID: 35998912

Henriksson L, Nurminen L, Hyvärinen A, Vanni S. 2008. Spatial frequency tuning in human retinotopic visual areas. *Journal of Vision* **8**:5. DOI: https://doi.org/10.1167/8.10.5, PMID: 19146347

Hertle RW, Yang D, Cochran M, Edward PR. 2017. Clinical contrast sensitivity function in patients with infantile nystagmus syndrome before and after eye muscle surgery. *Journal of Ophthalmology & Clinical Research* **4**:1–8. DOI: https://doi.org/10.24966/OCR-8887/100033

Himmelberg MM, Winawer J, Carrasco M. 2020. Stimulus-dependent contrast sensitivity asymmetries around the visual field. *Journal of Vision* **20**:18. DOI: https://doi.org/10.1167/jov.20.9.18, PMID: 32986805

Himmelberg MM, Winawer J, Carrasco M. 2023. Polar angle asymmetries in visual perception and neural architecture. *Trends in Neurosciences* **46**:445–458. DOI: https://doi.org/10.1016/j.tins.2023.03.006, PMID: 37031051

Horton JC, Hoyt WF. 1991. The representation of the visual field in human striate cortex. A revision of the classic Holmes map. *Archives of Ophthalmology* **109**:816–824. DOI: https://doi.org/10.1001/archopht.1991.01080060080030, PMID: 2043069

Kurzawski JW, Gulban OF, Jamison K, Winawer J, Kay K. 2022. Non-neural factors influencing BOLD response magnitudes within individual subjects. *The Journal of Neuroscience* **42**:7256–7266. DOI: https://doi.org/10.1523/JNEUROSCI.2532-21.2022, PMID: 35970558

Lange R, Kumagai A, Weiss S, Zaffke KB, Day S, Wicker D, Howson A, Jayasundera KT, Smolinski L, Hedlich C, Lee PP, Massof RW, Stelmack JA, Carlozzi NE, Ehrlich JR. 2021. Vision-related quality of life in adults with severe peripheral vision loss: A qualitative interview study. *Journal of Patient-Reported Outcomes* **5**:7. DOI: https://doi.org/10.1186/s41687-020-00281-y, PMID: 33439361

Lisboa R, Chun YS, Zangwill LM, Weinreb RN, Rosen PN, Liebmann JM, Girkin CA, Medeiros FA. 2013. Association between rates of binocular visual field loss and vision-related quality of life in patients with glaucoma. *JAMA Ophthalmology* **131**:486–494. DOI: https://doi.org/10.1001/jamaophthalmol.2013.2602, PMID: 23450425

Liu T, Heeger DJ, Carrasco M. 2006. Neural correlates of the visual vertical meridian asymmetry. *Journal of Vision* **6**:1294–1306. DOI: https://doi.org/10.1167/6.11.12, PMID: 17209736

Morales MU, Saker S, Wilde C, Pellizzari C, Pallikaris A, Notaroberto N, Rubinstein M, Rui C, Limoli P, Smolek MK, Amoaku WM. 2016. Reference clinical database for fixation stability metrics in normal subjects measured with the MAIA microperimeter. *Translational Vision Science & Technology* **5**:6. DOI: https://doi.org/10.1167/tvst.5.6.6

O'Connell C, Ho LC, Murphy MC, Conner IP, Wollstein G, Cham R, Chan KC. 2016. Structural and functional correlates of visual field asymmetry in the human brain by diffusion kurtosis MRI and functional MRI. *Neuroreport* **27**:1225–1231. DOI: https://doi.org/10.1097/WNR.0000000000000682, PMID: 27631541

Oliva A. 2005. CHAPTER 41—gist of the scene. In: Itti L, Rees G, Tsotsos JK (Eds). *Neurobiology of Attention*. Academic Press. p. 251–256. DOI: https://doi.org/10.1016/B978-012375731-9/50045-8

Pawloff M, Linhardt D, Woletz M, Hummer A, Sacu S, Vasileiadi M, Garikoitz LU, Holder G, Schmidt-Erfurth UM, Windischberger C, Ritter M. 2023. Comparison of stimulus types for retinotopic cortical mapping of macular disease. *Translational Vision Science & Technology* **12**:6. DOI: https://doi.org/10.1167/tvst.12.3.6, PMID: 36912591

Prabhakaran GT, Al-Nosairy KO, Tempelmann C, Thieme H, Hoffmann MB. 2021. Mapping visual field defects With fMRI. *Impact of Approach and Experimental Conditions. Frontiers in Neuroscience* **15**:745886. DOI: https://doi.org/10.3389/fnins.2021.745886, PMID: 34566575

Rai BB, Sabeti F, Carle CF, Maddess T. 2024. Visual field tests: A narrative review of different perimetric methods. *Journal of Clinical Medicine* **13**:2458. DOI: https://doi.org/10.3390/jcm13092458, PMID: 38730989

Randall D, Fox SL, Fenner JW, Arblaster GE, Bjerre A, Griffiths HJ. 2020. Using VR to investigate the relationship between visual acuity and severity of simulated Oscillopsia. *Current Eye Research* **45**:1611–1618. DOI: https://doi.org/10.1080/02713683.2020.1772834, PMID: 32546022

R Development Core Team. 2023. R: a language and environment for statistical computing. Vienna, Austria. R Foundation for Statistical Computing. https://www.R-project.org/

Ribeiro FL, Bollmann S, Puckett AM. 2021. Predicting the retinotopic organization of human visual cortex from anatomy using geometric deep learning. *NeuroImage* **244**:118624. DOI: https://doi.org/10.1016/j.neuroimage.2021.118624, PMID: 34607019

Ritter M, Hummer A, Ledolter AA, Holder GE, Windischberger C, Schmidt-Erfurth UM. 2019. Correspondence between retinotopic cortical mapping and conventional functional and morphological assessment of retinal

disease. *The British Journal of Ophthalmology* **103**:208–215. DOI: https://doi.org/10.1136/bjophthalmol-2017-311443, PMID: 29699983

Roelofzen C, Daghlian M, van Dijk JA, de Jong MC, Dumoulin SO. 2025. Modeling neural contrast sensitivity functions in human visual cortex. *Imaging Neuroscience* **3**:imag_a_00469. DOI: https://doi.org/10.1162/imag_a_00469, PMID: 40800939

Roh M, Selivanova A, Shin HJ, Miller JW, Jackson MI. 2018. Visual acuity and contrast sensitivity are two important factors affecting vision-related quality of life in advanced age-related macular degeneration. *PLOS ONE* **13**:e0196481. DOI: https://doi.org/10.1371/journal.pone.0196481, PMID: 29746512

Ross J, Morrone MC, Goldberg ME, Burr DC. 2001. Changes in visual perception at the time of saccades. *Trends in Neurosciences* **24**:113–121. DOI: https://doi.org/10.1016/s0166-2236(00)01685-4, PMID: 11164942

Rovamo J, Virsu V. 1979. An estimation and application of the human cortical magnification factor. *Experimental Brain Research* **37**:495–510. DOI: https://doi.org/10.1007/BF00236819, PMID: 520439

Rovamo J, Leinonen L, Laurinen P, Virsu V. 1984. Temporal integration and contrast sensitivity in foveal and peripheral vision. *Perception* **13**:665–674. DOI: https://doi.org/10.1068/p130665, PMID: 6543946

SamSrf. 2026. SamSrf. 10.36. GitHub. https://github.com/samsrf

Sereno MI, Dale AM, Reppas JB, Kwong KK, Belliveau JW, Brady TJ, Rosen BR, Tootell RBH. 1995. Borders of multiple visual areas in humans revealed by functional magnetic resonance imaging. *Science* **268**:889–893. DOI: https://doi.org/10.1126/science.7754376, PMID: 7754376

Subhi H, Latham K, Myint J, Crossland MD. 2017. Functional visual fields: relationship of visual field areas to self-reported function. *Ophthalmic & Physiological Optics* **37**:399–408. DOI: https://doi.org/10.1111/opo.12362, PMID: 28281282

Tailor VK, Theodorou M, Dahlmann-Noor AH, Dekker TM, Greenwood JA. 2021. Eye movements elevate crowding in idiopathic infantile nystagmus syndrome. *Journal of Vision* **21**:9. DOI: https://doi.org/10.1167/jov.21.13.9, PMID: 34935877

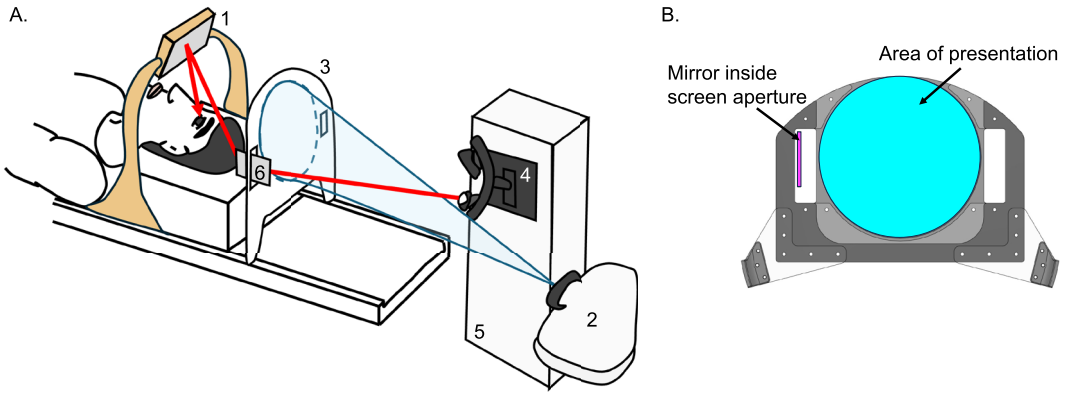
Welbourne LE, Morland AB, Wade AR. 2018. Population receptive field (pRF) measurements of chromatic responses in human visual cortex using fMRI. *NeuroImage* **167**:84–94. DOI: https://doi.org/10.1016/j.neuroimage.2017.11.022, PMID: 29155081

World Health Organization. 2019. WHO launches first World report on vision. https://www.who.int/news/item/08-10-2019-who-launches-first-world-report-on-vision [Accessed August 29, 2024].

Xu J, Moeller S, Auerbach EJ, Strupp J, Smith SM, Feinberg DA, Yacoub E, Uğurbil K. 2013. Evaluation of slice accelerations using multiband echo planar imaging at 3 T. *NeuroImage* **83**:991–1001. DOI: https://doi.org/10.1016/j.neuroimage.2013.07.055, PMID: 23899722

Appendix 1

A. Large-field setup



Appendix 1—figure 1. Schematic of large-field setup. (**A**) The participant lies on the scanner bed in the 64-channel coil without top to reduce obstruction and views the 40° screen via a mirror above their face (1). Stimuli are displayed using back-projection from a projector (2) outside the room, onto a screen (3) positioned behind the participant's head. The top of the screen follows the scanner bore curvature to maximize field of view. Monocular eye-tracking is achieved by mounting the illuminator and camera of the eye-tracker (4) vertically on a support (5) at the back of the scanner bore. An image of the eye is obtained via a dual-mirror setup, including a small mirror inside an aperture cut on the side of the screen (6) and the participant mirror (1). If the right eye is being tracked, the eye-tracker is placed on the left side of the scanner bore, and the eye-tracker mirror (6) is placed in the right screen aperture. (**B**) Schematic of the large-field screen, with the area of stimulus presentation shown in cyan and the mirror used for eye-tracking in magenta. The mirror is positioned within one of the two rectangular apertures cut on either side of the screen.

B. Individual level

To test for contrast sensitivity differences across the visual field in individual participants, we also employed a multilevel modeling approach using the lme4 package in R (***Bates et al., 2015***; ***R Development Core Team, 2023***). This approach reduces the impact of vertex-level variability and redundancy. The model included the square root of stimulus contrast as a continuous fixed-effect predictor, and eccentricity, polar location, and spatial frequency as categorical fixed-effect predictors, along with all possible interactions. Again, the intercept was fixed at 0. The model also included random slopes for the square root contrast and the interaction between square root contrast and voxel-specific factors and was fit separately for each participant. In the formula notation used in the R package lme4, the model would be defined as:

$$\beta \sim 0 + SqrtContrast + SqrtContrast:SF + SqrtContrast:Eccentricity +$$
$$SqrtContrast:PolarLocation + SqrtContrast:SF:Eccentricity +$$
$$SqrtContrast:SF:PolarLocation + SqrtContrast:Eccentricity:PolarLocation +$$
$$SqrtContrast:Eccentricity:PolarLocation:SF + (0 + SqrtContrast +$$
$$SqrtContrast:SF|VoxelIdx)$$

Appendix 1—table 1. Results from the multilevel modeling approach in each individual participant. pRF mapping was used to link brain responses to visual field locations.

SubID	Effects	Df	Sum Sq	Mean Sq	*F*-value	Pr(>*F*)	Signif.
	SF	1	3720	3720	72.49	<2e−16	***
	Eccentricity	1	35,003	35,003	681.995	<2e−16	***
	PolarLocation	3	11,258	3753	73.115	<2e−16	***
	SF:Eccentricity	1	23,914	23,914	465.938	<2e−16	***
	SF:PolarLocation	3	1546	515	10.041	1.32E−06	***
	Eccentricity:PolarLocation	3	200	67	1.297	0.274	
	SF:Eccentricity:PolarLocation	3	1158	386	7.519	5.04E−05	***
C1	Residuals	12,378	635,290	51			
	SF	1	23,704	23,704	743.628	<2e−16	***
	Eccentricity	1	13,503	13,503	423.609	<2e−16	***
	PolarLocation	3	46,442	15,481	485.647	<2e−16	***
	SF:Eccentricity	1	10,587	10,587	332.135	<2e−16	***
	SF:PolarLocation	3	2981	994	31.169	<2e−16	***
	Eccentricity:PolarLocation	3	2881	960	30.126	<2e−16	***
	SF:Eccentricity:PolarLocation	3	373	124	3.899	8.52E−03	**
C2	Residuals	11,604	369,897	32			
	SF	1	27	27	1.374	0.2411	
	Eccentricity	1	578	578	29.019	7.33E−08	***
	PolarLocation	3	7315	2438	122.52	<2e−16	***
	SF:Eccentricity	1	14,719	14,719	739.59	<2e−16	***
	SF:PolarLocation	3	257	86	4.311	4.80E−03	**
	Eccentricity:PolarLocation	3	2225	742	37.261	<2e−16	***
	SF:Eccentricity:PolarLocation	3	510	170	8.543	1.16E−05	***
C3	Residuals	9860	196,225	20			
	SF	1	25,290	25,290	521.73	<2e−16	***
	Eccentricity	1	3970	3970	81.89	<2e−16	***
	PolarLocation	3	34,475	11,492	237.08	<2e−16	***
	SF:Eccentricity	1	75,054	75,054	1548.38	<2e−16	***
	SF:PolarLocation	3	2514	838	17.29	3.40E−11	***
	Eccentricity:PolarLocation	3	16,417	5472	112.89	<2e−16	***
	SF:Eccentricity:PolarLocation	3	3921	1307	26.97	<2e−16	***
C4	Residuals	9896	479,688	48			
	SF	1	554	554	16.332	5.37E−05	***
	Eccentricity	1	6717	6717	198.161	<2e−16	***
	PolarLocation	3	886	295	8.711	9.12E−06	***
	SF:Eccentricity	1	13,436	13,436	396.384	<2e−16	***
	SF:PolarLocation	3	4753	1584	46.744	<2e−16	***
	Eccentricity:PolarLocation	3	3023	1008	29.727	<2e−16	***
	SF:Eccentricity:PolarLocation	3	2638	879	25.939	<2e−16	***
C5	Residuals	7728	261,956	34			

SubID	Effects	Df	Sum Sq	Mean Sq	*F*-value	Pr(>*F*)	Signif.
	SF	1	6008	6008	246.099	<2e−16	***
	Eccentricity	1	21,371	21,371	875.448	<2e−16	***
	PolarLocation	3	11,850	3950	161.806	<2e−16	***
	SF:Eccentricity	1	12,327	12,327	504.98	<2e−16	***
	SF:PolarLocation	3	714	238	9.745	2.04E−06	***
	Eccentricity:PolarLocation	3	1569	523	21.425	7.97E−14	***
	SF:Eccentricity:PolarLocation	3	762	254	10.409	7.80E−07	***
C6	Residuals	9360	228,493	24			
	SF	1	10,703	10,703	278.799	<2e−16	***
	Eccentricity	1	19,431	19,431	506.149	<2e−16	***
	PolarLocation	3	18,754	6251	162.84	<2e−16	***
	SF:Eccentricity	1	19,611	19,611	510.822	<2e−16	***
	SF:PolarLocation	3	153	51	1.325	2.64E−01	
	Eccentricity:PolarLocation	3	12,080	4027	104.885	<2e−16	***
	SF:Eccentricity:PolarLocation	3	1380	460	11.983	7.90E−08	***
C7	Residuals	10,794	414,384	38			

Signif. codes: 0 '***' 0.001 '**' 0.01 '*' 0.05 '.' 0.1 ' ' 1.

Appendix 1—table 2. Post hoc test on ANOVA visual quadrant position effect (PolarLocation) at the individual level.

pRF mapping was used to relate brain responses to visual field locations.

SubID	Effects	*contrast*	estimate	SE	df	t.ratio	p.value	
		HM > VM	5.5138156	0.3278444	12,354	16.818391	8.917786e−63	***
		LVM > UVM	0.5999187	0.2796053	12,354	2.145591	0.03192504	*
C1	PolarLocation	LHM > RHM	0.7058217	0.1711807	12,354	4.123254	3.759997e−05	***
		HM > VM	5.533751	0.2284595	11,580	24.22203	1.771783e−126	***
		LVM > UVM	4.387544	0.1852974	11,580	23.67839	4.420105e−121	***
C2	PolarLocation	LHM > RHM	2.288693	0.1336361	11,580	17.12630	5.942464e−65	***
		HM > VM	3.568024	0.2172194	9836	16.425896	7.786414e−60	***
		LVM > UVM	2.317875	0.1801032	9836	12.869704	1.339442e−37	***
C3	PolarLocation	LHM >RHM	0.159411	0.1214377	9836	1.312697	0.1893155	
		HM > VM	7.3408010	0.3070954	9872	23.903972	8.223761e−123	***
		LVM > UVM	3.1514598	0.2492052	9872	12.646043	2.250910e−36	***
C4	PolarLocation	LHM > RHM	–0.9417519	0.1794558	9872	–5.247821	1.571031e−07	***
		HM > VM	2.2997460	0.2874033	7704	8.001807	1.405261e-15	***
		LVM > UVM	0.2736311	0.2296279	7704	1.191628	0.2334437	
C5	PolarLocation	LHM > RHM	–0.2201730	0.1728344	7704	–1.273896	0.2027387	
		HM > VM	1.8040008	0.2259007	9336	7.985813	1.561107e−15	***
		LVM > UVM	3.2006411	0.1818476	9336	17.600678	3.057311e−68	***
C6	PolarLocation	LHM > RHM	0.3046082	0.1340245	9336	2.272779	0.02306211	*

Appendix 1—table 2 Continued on next page

Appendix 1—table 2 Continued

SubID	Effects	*contrast*	estimate	SE	df	t.ratio	p.value	
		HM >VM	5.9085493	0.3067623	10,770	19.261005	2.637528e−81	***
		LVM > UVM	2.0334164	0.2617710	10,770	7.767922	8.703410e−15	***
C7	PolarLocation	LHM > RHM	–0.3370417	0.1599345	10,770	–2.107373	0.03510831	*

Signif. codes: 0 '***' 0.001 '**' 0.01 '*' 0.05 '.' 0.1 ' ' 1.

C. Calibrated Benson Template

Appendix 1—table 3. Group-level ANOVA analysis on slope estimates, as function of spatial frequency, eccentricities, and visual quadrant positions.

The Benson template retinotopic map was used to relate brain responses to visual field locations.

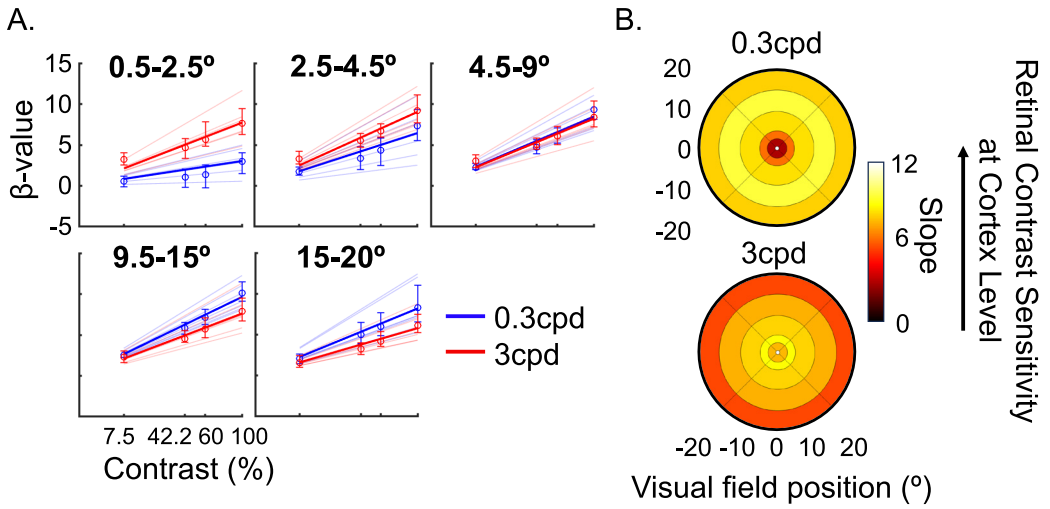
Measure of Interest: Slope	num Df	den Df	MSE	*F*	ges	Pr(>*F*)	
SF	1.0000	6.0000	31.436	0.6117	0.010887	0.4639018	
ECC	2.1650	12.9901	32.694	4.7020	0.160027	0.0270342	*
PolarLocation	1.7729	10.6374	27.316	7.0357	0.163209	0.0129521	*
SF:Eccentricity	2.2706	13.6238	7.438	29.4822	0.221807	7.552e−06	***
SF:PolarLocation	1.5885	9.5309	5.173	2.1025	0.009793	0.1783533	
Eccentricity: PolarLocation	12.0000	72.0000	5.253	2.9645	0.096634	0.0020990	**
SF: Eccentricity: PolarLocation	12.0000	72.0000	1.195	3.5212	0.028091	0.0003995	***

Signif. codes: 0 '***' 0.001 '**' 0.01 '*' 0.05 '.' 0.1 ' ' 1.

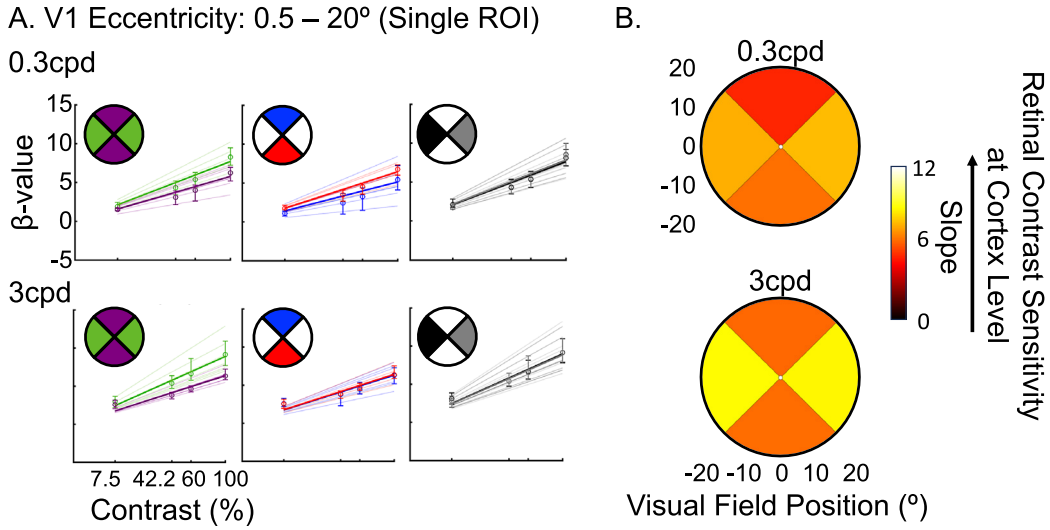
Appendix 1—table 4. Post hoc *t*-test analysis for the visual quadrant position effect (PolarLocation) and the interaction between spatial frequency and eccentricities (SF:Eccentricity) reported in Appendix 1—table 3.

The Benson template retinotopic map was used to relate brain responses to visual field locations.

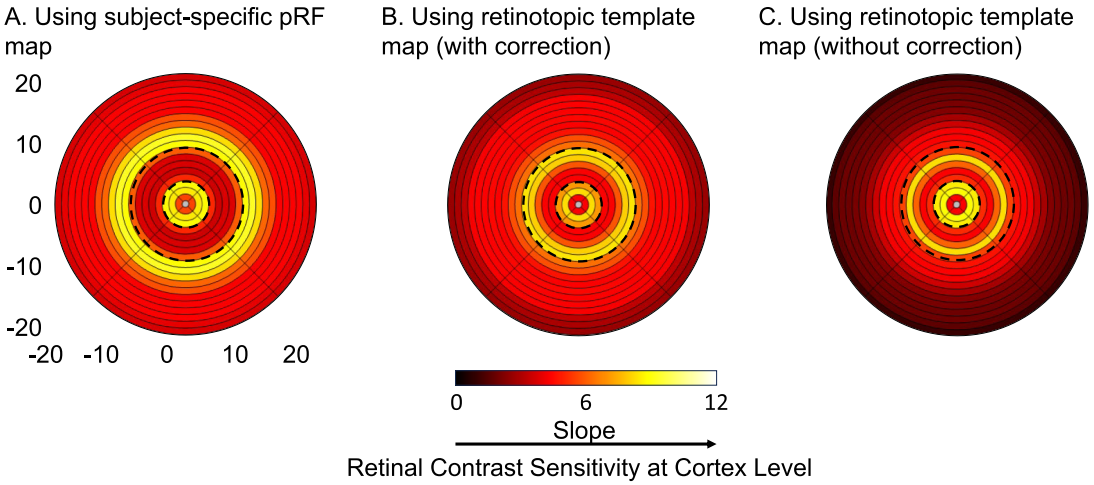
Measure of Interest: Slope	contrast	estimate	SE	df	t.ratio	p.value
	Horizontal > Vertical	4.3378240	1.2101752	6	3.5844596	0.01158079
	Lower > Upper	0.5249520	0.7053736	6	0.7442184	0.48485944
PolarLocation	Left > Right	–0.2265194	0.3922638	6	–0.5774671	0.58462631
	3–0.3 cpd: 0.5°–2.5°	4.5917619	0.7960846	6	5.7679320	0.001185113
	3–0.3 cpd: 2.5°–4.5°	2.5801243	1.0192745	6	2.5313340	0.044599322
	3–0.3 cpd: 4.5°–9.5°	–0.2927635	0.9981812	6	–0.2932969	0.779175269
	3–0.3 cpd: 9.5°–15°	–1.9782789	0.6042727	6	–3.2738182	0.016953076
SF:Eccentricity	3–0.3 cpd: 15°–20°	–2.2803080	0.6462658	6	–3.5284368	0.012391168



Appendix 1—figure 2. V1 contrast sensitivity (i.e., slopes) across five eccentricity bins (0.5°–2.5°, 2.5°–4.5°, 4.5°–9.5°, 9.5°–15°, and 15–20°), defined using the calibrated Benson atlas. (**A**) *β*-values versus contrast levels for each eccentricity bin. Blue and red lines represent the contrast sensitivity model fits for the 0.3 and 3cpd conditions, respectively. Thick lines represent the group-level model fit (n=7), thin lines correspond to individual fits. (**B**) V1 contrast sensitivity index (i.e., slope) projected back into the visual space using the calibrated Benson atlas, for each eccentricity bin and spatial frequency condition. The color scale indicates slope estimates, with higher values representing higher V1 contrast sensitivity.



Appendix 1—figure 3. V1 contrast sensitivity (i.e., slopes) across visual field quadrants using the calibrated Benson atlas, for the 0.3 and 3 cpd conditions. Visual quadrants were defined as ±45° regions around the cardinal meridians, and slope values were selected for eccentricities between 0.5° and 20°. Horizontal quadrants are left and right, while upper and lower quadrants define the vertical quadrants. (**A**) β-values versus contrast levels for each anisotropy effect: horizontal versus vertical, upper versus lower, and left versus right. Thick lines represent group-level model fits (n=7), thin lines correspond to individual fits. Error bars represent the 95% confidence intervals. (**B**) V1 contrast sensitivity index (i.e., slope) projected back into the upper, lower, left, and right visual field quadrants for the 0.3 and 3 cpd conditions. The color scale represents slope estimates, with higher values indicating higher V1 contrast sensitivity.



Appendix 1—figure 4. Effect of correcting eccentricity distribution in retinotopic templates on cortical contrast sensitivity maps. Heatmaps show slope values back projected into visual space, with each concentric circle representing a 1° eccentricity bin. (**A**) Back projection was performed using subject-specific pRF map, (**B**) Using Benson atlas with eccentricity distribution corrected using the H&H model. (**C**) Using Benson atlas without correction (original template). Color scale indicates slope values reflecting cortical contrast sensitivity (brighter = larger slopes).